

Chapter 3

Charge Transfer Rates

This chapter focuses on the influence of different components in charge transfer rates, mainly in terms of applicability for charge transport simulations in mesoscopic, amorphous materials. In particular, we compare different methods to determine the charge transfer integral (Sec. 3.1), the internal reorganization energy and site energy difference (Sec. 3.2), and the hopping site distance (Sec. 3.3) to finally compare different theoretical approaches for rate types (Sec. 3.4). (See Comp. Details 2.1)

3.1 Charge Transfer Integral

In the next section we discuss the evaluation of the charge transfer integral $|J_{AB}|$. We study $|J_{AB}|$ for the stacking aggregates of DIPBI molecules (Sec. 3.1.1). Furthermore, the partitioning of the P3MT polymer chain into segments and comparison to the treatment in P3HT including the side chains is discussed (Sec. 3.1.2). The chain length dependence of $|J_{AB}|$ in coplanar P3MT chains is analysed.

More technical issues are the dependence of the charge transfer integral on the selected computational method (functional, basis set), the impact of the selected method on the distribution for pairs in the morphology (Sec. 3.1.3), the scaling of various methods for hole and electron transfer in P3MT and DIPBI (Sec. 3.1.4) or the determination of $|J_{AB}|$ as a function of geometric parameters (Sec. 3.1.5). An alternative approach to determine $|J_{AB}|$ is a scaling of the overlap $|S_{AB}|$ for different method (Sec. 3.1.6).

3.1.1 Evaluation for DIPBI Dimers within CDFT and DIPRO

In the following, we discuss the CDFT (Sec. 1.2.2.5) and DIPRO/DFT (Sec. 1.4.3.1) results for the charge transfer integral $|J_{AB}|$ in an optimised DIPBI dimer configuration for the electronic ground state S_0 (Fig. 3.1,i). Suppose a negative charge is localised on the dimer structure and the wavefunction is optimised in a self-consistent field calculation with DFT/PBE/80Ry. In that case, the highest single occupied molecular orbital is delocalised over both monomer DIPBI structures in dimer configuration (Fig. 3.1,ii). The introduction of the CDFT constrain localises the excess charge on the donor (iii) or the acceptor (iv) part of the charge-transfer complex.

Charge transfer integral for electron transfer $|J_{AB}^e| = 7.73 \times 10^{-2}$ eV is about a factor 28 higher than the value for hole transfer $|J_{AB}^h| = 2.73 \times 10^{-3}$ eV. The overlap for electron transfer is $|S_{AB}^e| = 1.95 \times 10^{-1}$, about one order of magnitude higher than the corresponding overlap for hole transfer $|S_{AB}^h| = 1.97 \times 10^{-2}$.

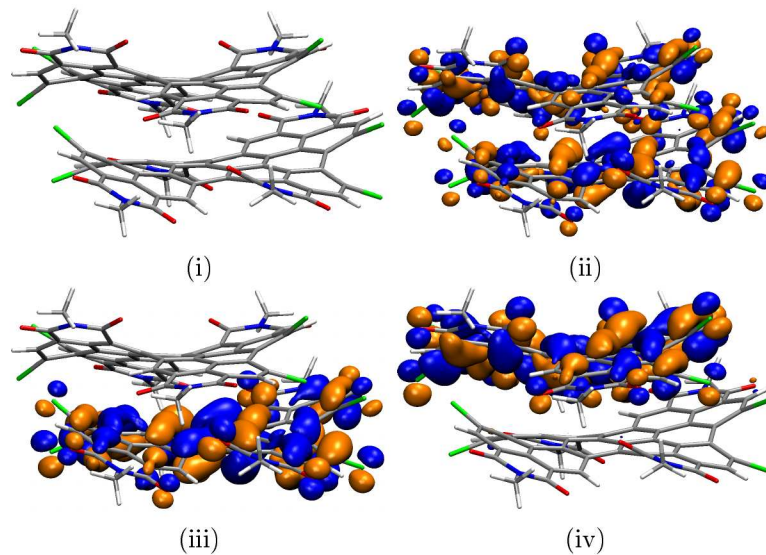


Figure 3.1: (i) The underlying structure is optimised in the neutral ground state S_0 on PBE0-D3(BJ)/6-31G* level of theory. (ii) Isodensity plot of the highest single occupied molecular orbital with an excess charge on the DIPBI dimer with DFT/PBE/80Ry, with constraints and an excess charge localised on the donor (iii) and acceptor molecule (iv) with CDFT/PBE/80Ry.

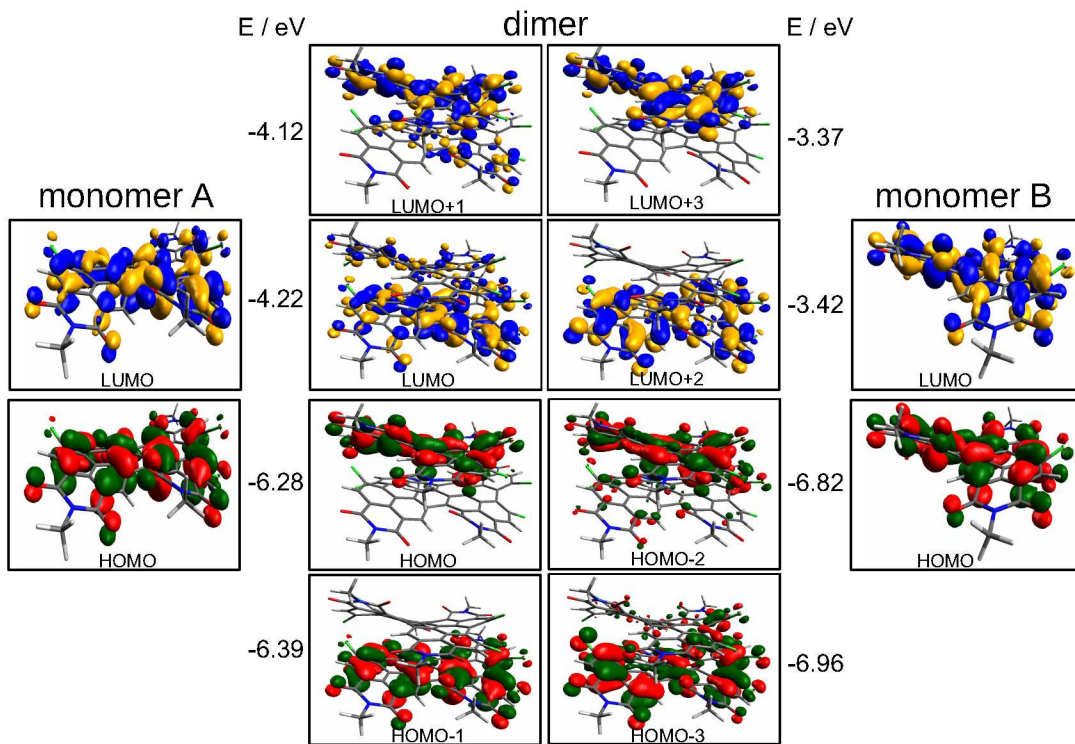


Figure 3.2: Schematic representation of frontier orbitals involved in the DIPRO/PBE0-D3(BJ)/6-31G* calculation for a DIPBI dimer at the optimised neutral ground state S_0 geometry. The figure displays the involved HOMOs for hole transfer (red) and the LUMOs for electron transfer (blue) on the isolated monomers A (left) and B (right) in the dimer configuration (middle) with a subset of dimer frontier orbitals (HOMO-3 to LUMO+3). Furthermore, the corresponding Kohn-Sham energy eigenvalues E for the dimer are depicted. In the DIPRO calculation, the monomer orbitals are projected on the dimer orbitals and prorated by the Kohn-Sham energies to determine the charge transfer integral $|J_{AB}|$.

An alternative approach to determine $|J_{AB}|$ is using the dimer projection method. At the optimised PBE0-D3(BJ)/6-31G* dimer configuration the charge transfer integral for an electron with DIPRO/PBE0/6-31G* is $|J_{AB}^e| = 4.26 \times 10^{-2}$ eV, which is slightly lower than the CDFT reference value, but at the same order of magnitude. The corresponding $|J_{AB}^h| = 3.89 \times 10^{-3}$ eV for hole transfer is about one order of magnitude lower, which is in line with the trends for CDFT. The overlap from LUMO A to LUMO B transition used in the DIPRO calculation for electron transfer is $|S_{AB}^e| = 5.05 \times 10^{-3}$ and the HOMO A to HOMO B transfer is $|S_{AB}^h| = 1.42 \times 10^{-3}$.

The predominantly involved frontier orbitals in the DIPRO calculation are depicted in Figure 3.2. The schema displays the HOMOs for hole transfer and the LUMOs for electron transfer on the isolated monomers A and B in the dimer configuration and a selection of dimer frontier orbitals. The HOMO in monomer A is similar to HOMO-1 in the dimer, and the HOMO in monomer B corresponds to the dimer HOMO. Moreover, the dimer orbitals exhibit contributions on both monomers.

Visual inspection of the orbitals and the evaluated overlap detail that the restriction to the frontier orbitals in the DIPRO method is a suitable approximation to the CDFT reference, where the latter method represents the physical situation more accurately.

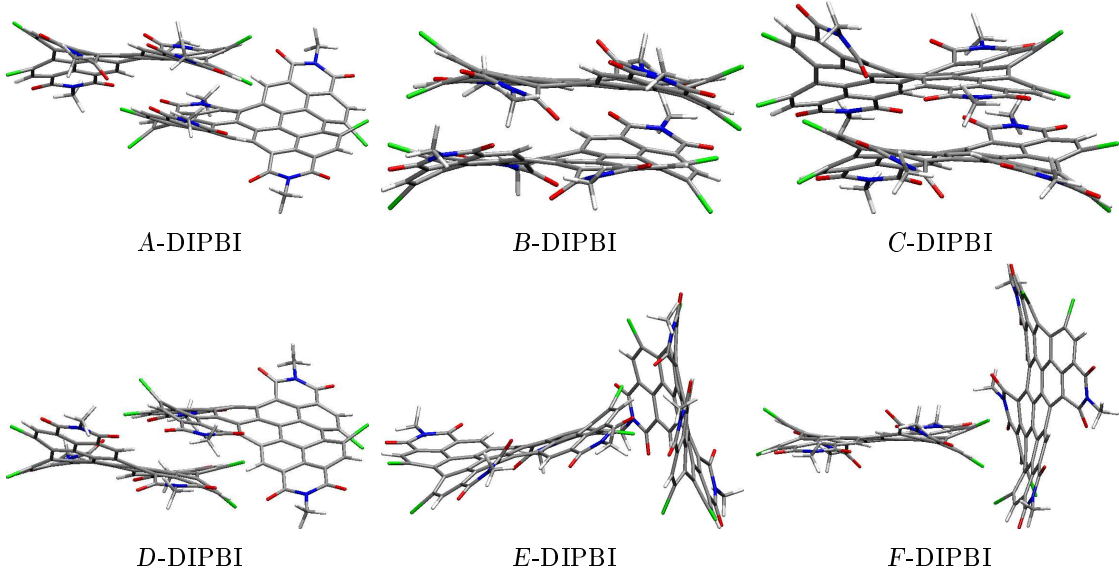


Figure 3.3: The optimised the neutral ground state S_0 DIPBI dimer structures on B3LYP-D3(BJ)/6-31G* level of theory (A-F).

In the following, we focus on how the molecular arrangement influences charge transfer properties like $|J_{AB}^{h/e}|$, $|S_{AB}^{h/e}|$ and $k_{AB}^{h/e}$ between DIPBI dimers. As the relative orientation of two molecules can vary when forming dimers, DFT-based ground state S_0 geometry optimisations are performed to get an ensemble of six dimer structures, which correspond to local minima on the potential energy surface (B3LYP-D3(BJ)/6-31G**). The obtained DIPBI dimer structures (A-F) exhibit different aggregation alignments (Fig. 3.3). A-DIPBI is the lowest structure in energy and yields a partial overlap of both DIPBI planes, where one PDI unit participates in the formation of π -stacks from each monomer. In B-DIPBI and C-DIPBI, the monomers form π -stacks, where both DIPBI planes yield a face-on orientation. One PDI unit of the first monomer is roughly centred between the PDI units of the adjacent monomer. The monomers yield a higher lateral shift in C-DIPBI than in B-DIPBI.

The stacking in *D*-DIPBI is similar to *A*-DIPBI, but the monomers yield slightly different curvature with respect to each other. The dimer configurations *E*-DIPBI and *F*-DIPBI yield T-stack aggregation patterns, where both DIPBI planes are oriented roughly orthogonal to each other.

We find $|J_{AB}^e| = 5.29 \times 10^{-3}$ eV and $|J_{AB}^h| = 5.60 \times 10^{-2}$ eV for *A*-DIPBI and for the ensemble average $|\bar{J}_{AB}^e| = (1.72 \pm 2.24) \times 10^{-2}$ eV and $|\bar{J}_{AB}^h| = (2.22 \pm 2.65) \times 10^{-2}$ eV (Tab. 3.1). Taken together, these values lead to an average Marcus rate for electron transfer $\bar{k}_{AB}^e = (9.68 \pm 19.73) \times 10^{12}$ s⁻¹, which is enhanced with respect to the hole transfer rate $\bar{k}_{AB}^h = (2.33 \pm 3.35) \times 10^{12}$ s⁻¹ in homo-molecular DIPBI dimers.

Table 3.1: Relative ground state energy $E_{\text{rel}}(S_0)$, charge transfer integral $|J_{AB}|$ (DIPRO/B3LYP/6-31G*), frontier molecular orbital overlap $|S_{AB}|$, Marcus charge transfer rate k_{AB} for electron and hole transfer in DIPBI dimers. The rates k_{AB} are evaluated at a temperature of $T = 300$ K with an external field $|\mathbf{F}^{\text{ext}}| = 1.0 \times 10^8$ V m aligned parallel to the centre of mass connection vector d_{COM} . $\Delta E^{\text{out}} = 0.0$ eV, $\lambda^{\text{out}} = 0.0$ eV. The DIPBI dimer structures (*A*-*F*) are optimised at the neutral ground state S_0 at B3LYP-D3(BJ)/6-31G* level of theory.

	<i>A</i>	<i>B</i>	<i>C</i>	<i>D</i>	<i>E</i>	<i>F</i>
$E_{\text{rel}}(S_0)$ / eV	0.00	0.26	0.34	1.19	2.22	2.45
$ J_{AB}^e $ / eV	5.29E-3	6.27E-2	9.82E-3	5.29E-3	9.94E-3	8.04E-4
$ J_{AB}^h $ / eV	5.60E-2	1.17E-2	6.54E-3	5.60E-2	1.44E-3	6.54E-4
$ S_{AB}^e $	1.81E-3	7.29E-3	6.22E-4	1.81E-3	1.13E-3	4.73E-4
$ S_{AB}^h $	6.87E-3	1.02E-3	3.89E-4	6.87E-3	9.08E-5	3.28E-5
k_{AB}^e / s ⁻¹	5.22E+11	4.99E+13	2.19E+12	5.22E+11	2.48E+12	3.91E+11
k_{AB}^h / s ⁻¹	6.64E+12	6.72E+11	5.02E+10	6.64E+12	1.67E+9	8.79E+8

In the P3HT:DIPBI morphology the aggregated dimer configurations can differ significantly with respect to the optimised ground state configurations, as the aggregation process depends on the annealing process. Therefore, an ensemble of 10 dimer structures from the 500 K morphology is presented. The ensemble averaged charge transfer integrals for electron $|\bar{J}_{AB}^e| = (4.88 \pm 8.23) \times 10^{-3}$ eV and hole transfer $|\bar{J}_{AB}^h| = (3.81 \pm 5.95) \times 10^{-3}$ eV are approximately one order of magnitude lower than for optimised structures.

This trend is also found for the averaged overlap $|\bar{S}_{AB}^h| = (4.29 \pm 6.05) \times 10^{-4}$ and $|\bar{S}_{AB}^e| = (1.01 \pm 4.60) \times 10^{-4}$, and results in a reduction of the averaged charge transfer rates $\bar{k}_{AB}^e = (2.31 \pm 5.29) \times 10^{12}$ s⁻¹ and $\bar{k}_{AB}^h = (8.15 \pm 20.02) \times 10^{10}$ s⁻¹ when compared to DFT-optimised ground state dimer configurations. One should keep in mind this tendency of lower charge transfer properties of force-field generated structures compared to DFT-optimised pairs, if we compare the results for DFT-based acceptor dimers (Sec. 5).

3.1.2 P3MT Polymer Chain Partitioning in the Amorphous Phase

A pair of neighbouring P3MT polymer chains with chain segment length $n=32$ is depicted in Figure 3.4 as an outtake from the P3HT:DIPBI morphology. The chains show two interchain junctions for a possible interchain charge transfer. One can see that the frontier orbitals like HOMO and LUMO are not delocalised along the entire polymer chain but only localised on several thiophene subunits (Fig. 3.4,i,ii).

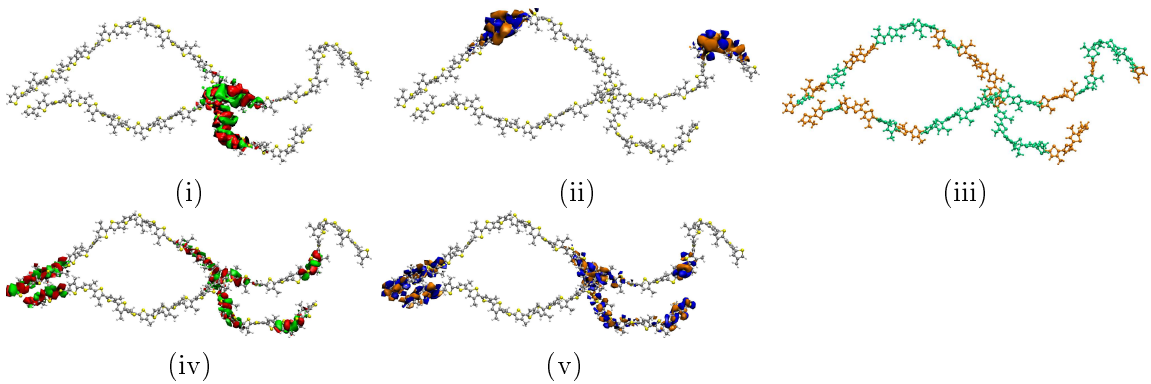


Figure 3.4: The localisation of frontier orbitals at a pair of two P3MT chains with a segment length $n=32$ for (i) the HOMO (red, green) and (ii) the LUMO (blue, orange).

Partitioning of two P3MT chains into segments (orange, cyan) at a cutoff angle $\theta_{\text{SCCS}}^{\text{cut}} = 75^\circ$ (iii). (iv) Frontier orbitals HOMOs (red, green) and (v) LUMOs (blue, orange) involved in interchain transitions (B3LYP/6-31G*).

If one evaluates the charge transfer integral between the entire $n=32$ polymer P3MT chains, one obtains only a significant value for hole transfer $|J_{\text{AB}}^{\text{h}}| = 1.97 \times 10^{-3}$ eV, as the HOMOs are localised for both monomers at the intermolecular junction site, whereas the charge transfer integral for electron transfer is negligible $|J_{\text{AB}}^{\text{e}}| = 2.05 \times 10^{-11}$ eV for a LUMO A to LUMO B transitions, as the involved orbitals are located far apart from each other. This finding is also reflected in the frontier orbital overlap for hole transfer $|S_{\text{AB}}^{\text{h}}| = 4.24 \times 10^{-4}$ and the corresponding tiny value for electron transfer $|S_{\text{AB}}^{\text{e}}| = 3.80 \times 10^{-12}$. Hence, the resulting DIPRO charge transfer integral for electron transfer and the associated Marcus rate drop to zero.

One can overcome this deficiency, if the polymer chain is partitioned into segments (Fig. 3.4,iii). Therefore a cutoff dihedral angle $\theta_{\text{SCCS}}^{\text{cut}}$ between neighbouring SCCS atoms is introduced. This entails an *a priori* selection of the conjugated segments, that represent the hopping sites in the kMC simulations. Here, a cutoff dihedral angle $\theta_{\text{SCCS}}^{\text{cut}} = 75^\circ$ is applied. The segments are saturated with virtual H atoms in the DIPRO calculations for the charge transfer integral, that incorporate the localisation and shape of the DFT-based frontier orbital.

The partitioning leads to twelve conjugated segments on the first chain and thirteen on the second chain. The segment length is between $n=1$ and 10 thiophene subunits. The HOMOs and LUMOs are located at the segments, which are in close proximity (Fig. 3.4,iv,v), and the corresponding Marcus rates yield nine possible interchain transitions with non-negligible contributions. Averaging all interchain transitions leads to $|\bar{J}_{\text{AB}}^{\text{h}}| = (4.80 \pm 5.71) \times 10^{-3}$ eV for hole transfer and higher values for electron transfer $|\bar{J}_{\text{AB}}^{\text{e}}| = (1.76 \pm 2.80) \times 10^{-2}$ eV. This trend is also reflected in the averaged overlap $|\bar{S}_{\text{AB}}^{\text{h}}| = (6.58 \pm 9.62) \times 10^{-4}$ and $|\bar{S}_{\text{AB}}^{\text{e}}| = (1.97 \pm 2.91) \times 10^{-3}$.

Comparison of the frontier orbitals including the side chains in P3HT with partitioning (Fig. 3.5,i,ii) yields a similar localisation as for the P3MT polymer chains (Fig. 3.4,iv,v), as the side chains do not affect the frontier orbital localisation on the polymer backbone. Averaging all interchain transitions leads to $|\bar{J}_{\text{AB}}^{\text{h}}| = (5.26 \pm 8.58) \times 10^{-3}$ eV and $|\bar{J}_{\text{AB}}^{\text{e}}| = (1.71 \pm 2.80) \times 10^{-3}$ eV for this pair of P3HT chains using DIPRO/B3LYP/6-31G*. The averaged overlap is $|\bar{S}_{\text{AB}}^{\text{h}}| = (7.27 \pm 13.9) \times 10^{-4}$ for hole transfer and $|\bar{S}_{\text{AB}}^{\text{e}}| = (1.84 \pm 2.92) \times 10^{-3}$ for electron transfer.

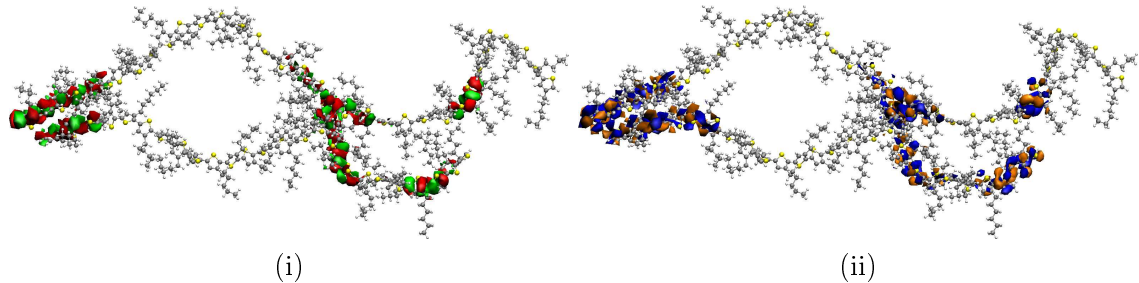


Figure 3.5: Localisation of frontier orbitals HOMOs (i) and LUMOs (ii) involved in inter-chain transitions for a pair of P3HT chains including aliphatic side chains. The chains were extracted from the P3HT:DIPBI morphology partitioned into conjugated segments with $\theta_{\text{SCCS}}^{\text{cut}} = 75^\circ$ (B3LYP/6-31G*). The reduction of the P3HT segment to a P3MT segment does not significantly alter the frontier orbital localisation (see Fig. 3.4).

The $|\bar{J}_{AB}|$ and $|\bar{S}_{AB}|$ in P3MT do not deviate significantly from the results in P3HT, which entails the validity of the reduction of the side chains to methyl groups in the evaluation of the charge transfer integral with DIPRO, which reduces computational costs.

The data for the electron transfer in this configuration details variations in $|J_{AB}|$ at about nine orders of magnitude. Hence, it is crucial that the frontier orbitals are localised at the chain junctions. Therefore, the polymer chain is divided into smaller segments that reflect the delocalisation of the excess charge in the conjugated π -system, and their $|J_{AB}|$ are applied in the intermolecular charge transfer rates between neighbouring chains.

The distribution of the intermolecular charge transfer integrals in the P3HT:DIPBI morphology depend on the segmentation of the polymer chains inside the morphology (Fig. 3.6). At a first glance, the normalised distributions of the charge transfer integrals do not differ significantly as a function of the cutoff angle θ_{cut} (Eq. 268). Nevertheless, one needs to keep in mind, that the number of displayed pairs varies significantly, e.g. 3.1×10^5 pairs at $\theta_{\text{cut}} = 0^\circ$, which refers to a segmentation at every thiophene unit, 1.0×10^5 pairs at $\theta_{\text{cut}} = 75^\circ$ and 4.1×10^3 pairs at $\theta_{\text{cut}} = 90^\circ$ for P3HT at $n = 32$. As the cutoff radius for the inclusion of neighbouring pairs is fixed $r_{\text{cut}}^{\text{pairs}}$, the amount of pairs with negligible, small $|J_{AB}|$ increases for smaller θ_{cut} and hence the distributions appear shallower. These features repeat for electrons to the same extend as they do for the holes. In general, we observe a higher number of pairs, where the charge transfer integral for holes is higher than the corresponding value for electrons ($|J_{AB}^h| > |J_{AB}^e|$). For $\theta_{\text{cut}} = 0^\circ$, we find in 70% cases a higher $|J_{AB}^h|$, whereas this quota shrinks gradually with increasing cutoff angle as $\theta_{\text{cut}} = 75^\circ$ yields 64% and declines to 53% for $\theta_{\text{cut}} = 90^\circ$.

Charge transfer integral between linear P3MT chains The square of the charge transfer integral $|J_{AB}|^2$ in P3MT as a function of the polymer chain length n for the thiophene units displays a decay with increasing n (Fig. 3.7). The selected P3MT dimer structures are planar, parallel aligned segments at constant distances $d_{\text{COM}} = 4.0 \text{ \AA}$ with an alternating orientation of the side-chain groups. In the DIPRO approach the electron transfer is approximated as a LUMO A to LUMO B transition and yields higher values for interchain electron transfer integral than for hole transfer. In the same way, a HOMO A to HOMO B transition is assumed for hole transfer in the DIPRO calculations on B3LYP/6-31G* level of theory. The charge transfer integral decays with a factor four for small chain length $n \leq 5$ and is attenuated for polymer chains with higher n .

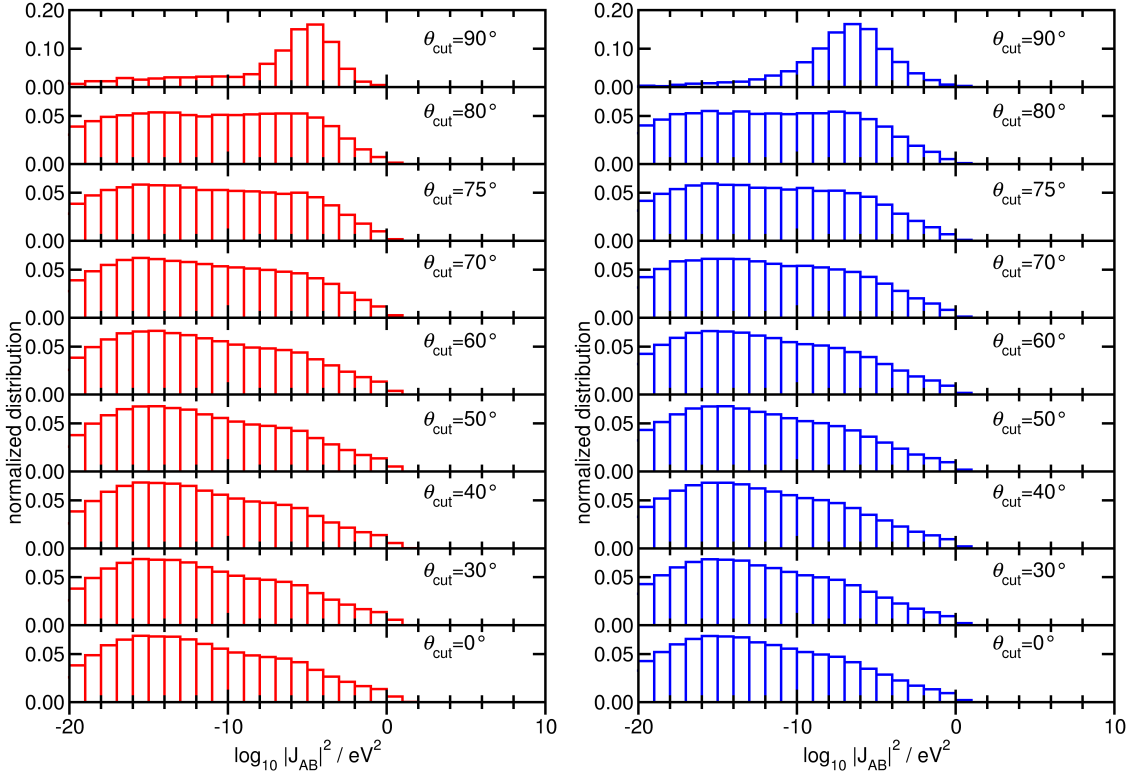


Figure 3.6: Normalised distributions of ZINDO/MOO charge transfer integrals as a function of the cutoff SCCS dihedral angle θ_{cut} for the partitioning of the polymer chains inside the P3HT:DIPBI morphology. Charge transfer pairs are included in the distributions, if the distance d_{COM} is within a cutoff radius $r_{\text{cut}}^{\text{pairs}} = 1.3 \text{ nm}$ for hole transfer (red) and for electron transfer (blue), respectively. The histograms include, e.g. 3.1×10^5 pairs at $\theta_{\text{cut}} = 0^\circ$, which refers to the segmentation at every thiophene unit, 1.0×10^5 pairs at $\theta_{\text{cut}} = 75^\circ$ and 4.1×10^3 pairs at $\theta_{\text{cut}} = 90^\circ$ for P3HT 32mers.

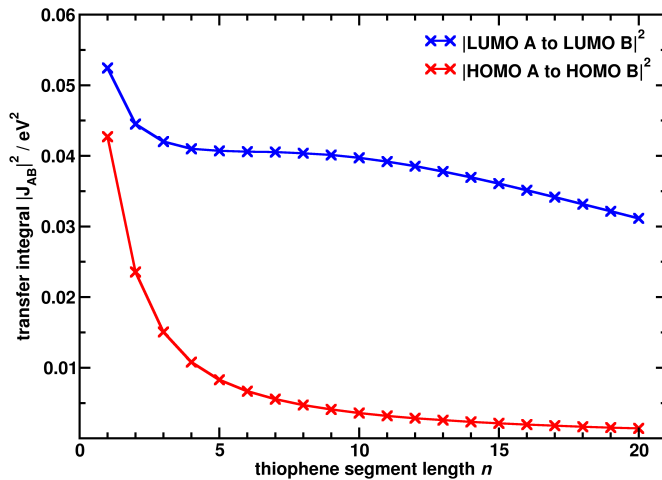


Figure 3.7: Charge transfer integral $|J_{AB}|^2$ in P3MT as a function of the polymer chain length n . The electron transfer is regarded as LUMO A to LUMO B transition in the P3MT dimer configuration and hole transfer as HOMO A to HOMO B for the DIPRO charge transfer integral on B3LYP/6-31G* level of theory. The P3MT dimers are generated as planar, parallel aligned segments at a constant distances $d_{\text{COM}} = 4.0 \text{ \AA}$. The charge transfer integral $|J_{AB}|^2$ decreases with an increasing polymer chain length n .

3.1.3 Comparing Different Evaluation Methods

As the charge transfer integral $|J_{AB}|$ is a key quantity in the Marcus rate expression the dependence of the DIPRO method on the functional and basis set matters (Fig. 3.8). For the selected pair of two P3MT polymer chains with a thiophene segment length $n=32$, the DIPRO/ZINDO approach results in the lowest value for the charge transfer integral. The semiempirical methods AM1 and PM3 yield similar results and show a good agreement with the DFT-based data and a small basis set like B3LYP/3-21G, B3LYP/4-31G or PBE/3-21G. The augmentation of the basis set with the introduction of additional polarisation functions (indicated by the symbol *), only introduces a slight reduction in $|J_{AB}|$, e.g. for comparison of B3LYP/6-31G and B3LYP/6-31G*. An increase in the basis set size leads in this configuration to a higher $|J_{AB}|$, e.g. for B3LYP/3-21G*, B3LYP/6-31G*, B3LYP/6-311G*, B3LYP/6-311G**. If a large basis set is selected like 6-311G**, the differences in the results for different functionals like B3LYP, BP86, PBE0, PBE is negligible. The incorporation of long-range effects in the functional as for LC-BLYP or the range-separated functional CAM-B3LYP leads to a decrease of $|J_{AB}|$. In total, we see that the value for charge transfer integral can vary about one order of magnitude as a function of the basis set and the functional, provided that the localisation of the frontier orbitals is maintained at the intermolecular junction. The comparison indicates that the choice of a sufficiently large basis set is more crucial than the choice of the functional to determine $|J_{AB}|$.

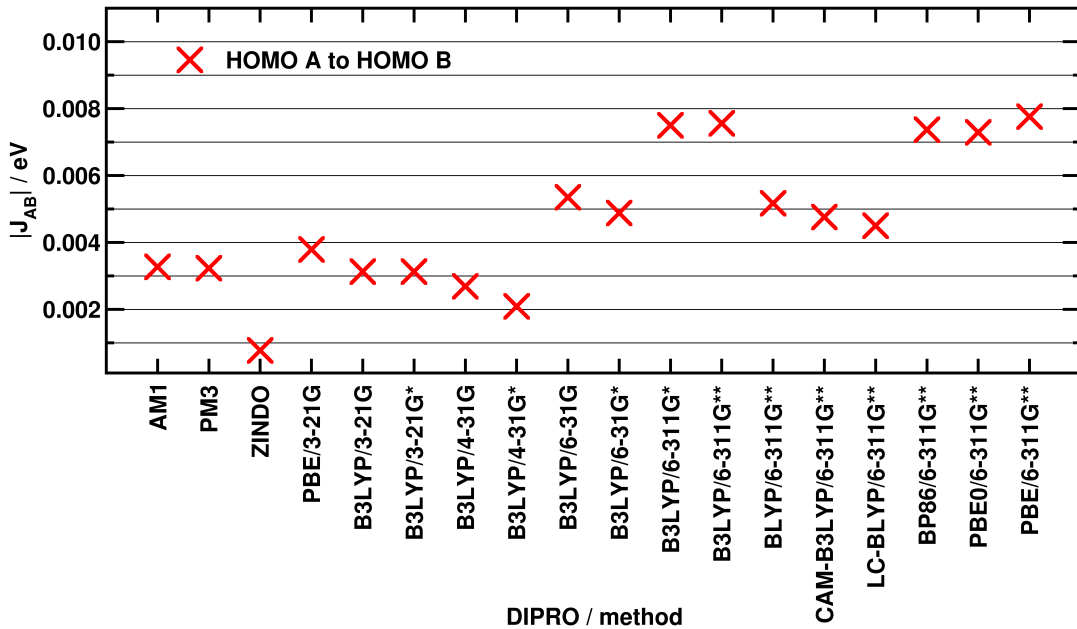


Figure 3.8: Charge transfer integral $|J_{AB}|$ in P3MT for a pair of two neighbouring polymer $n=32$ chains, with two linking sites for charge transfer. The hole transfer is treated as a HOMO A to HOMO B transition with the DIPRO approach for different functionals and basis sets or semiempirical methods AM1, ZINDO and PM3.

Distribution of the Charge Transfer Integral in P3HT Morphology In the following, we take a look at the charge transfer integrals in an entire frame of the morphology. We compare the ZINDO/MOO method and the DIPRO approach in conjugation with B3LYP/6-31G*, DFTB/3OB or different semiempirical methods PM3, AM1, ZINDO.

Therefore, we apply the partitioning schema with $\theta_{\text{cut}} = 75^\circ$ to the amorphous P3HT morphology (Eq. 268) and determine the charge transfer integrals for the $N^{\text{NN}} = 12$ nearest neighbours.

The distributions of the charge transfer integrals are depicted in Figure 3.9. They vary significantly in their shape, the average values and the standard deviation depending on the underlying electronic structure method. The average $\log_{10} |\bar{J}_{AB}|^2 = (-14.15 \pm 8.79) \text{ eV}^2$ for ZINDO/MOO is the lowest value and the method exhibits the broadest distribution. The DIPRO-based charge transfer integrals yield significantly higher averages. For instance, the mean for DIPRO/ZINDO $\log_{10} |\bar{J}_{AB}|^2 = (-9.96 \pm 4.52) \text{ eV}^2$ is shifted about four orders of magnitude with respect to ZINDO/MOO. The DIPRO/B3LYP/6-31G* data is centred at $\log_{10} |\bar{J}_{AB}|^2 = (-9.22 \pm 4.67) \text{ eV}^2$. The distribution for DIPRO/DFTB yields a different shape with two accumulation points and the smallest width. The average for DIPRO/DFTB is $\log_{10} |\bar{J}_{AB}|^2 = (-8.02 \pm 3.07) \text{ eV}^2$, which is below both values for DIPRO/AM1 (-7.58 ± 5.15) eV^2 and DIPRO/PM3 (-6.38 ± 5.54) eV^2 . The centres of the DIPRO distribution differ up to four orders of magnitude. Comparison of the computational cheap data sets with the demanding DIPRO/B3LYP/6-31G* approach shows that DIPRO/ZINDO yields the best agreement with the DFT-based data.

As $|J_{AB}|$ is a key property in charge transfer rates, the choice of the calculation method significantly influences the magnitude of the rates and hence also alters the simulated charge carrier mobility (see Sec. 4.1.2.1). Even though the ZINDO/MOO is widely used in literature [190, 282], the enormous deviations from the more computationally demanding but more accurate DIPRO results rise doubts in the applicability to amorphous polymers like P3HT. The failure of ZINDO/MOO is not surprising, as we only employ a single ZINDO reference calculation on an isolated, flat segment for every thiophene segment length n . This way one cannot cover the large conformational space of P3HT chain configurations, which is found in the amorphous phase. Moreover, the results for distinct DIPRO-based $|J_{AB}|$ yield high deviations as well, hence we need more accurate reference data and we introduce a scaling scheme to compare the methods (Sec. 3.1.4).

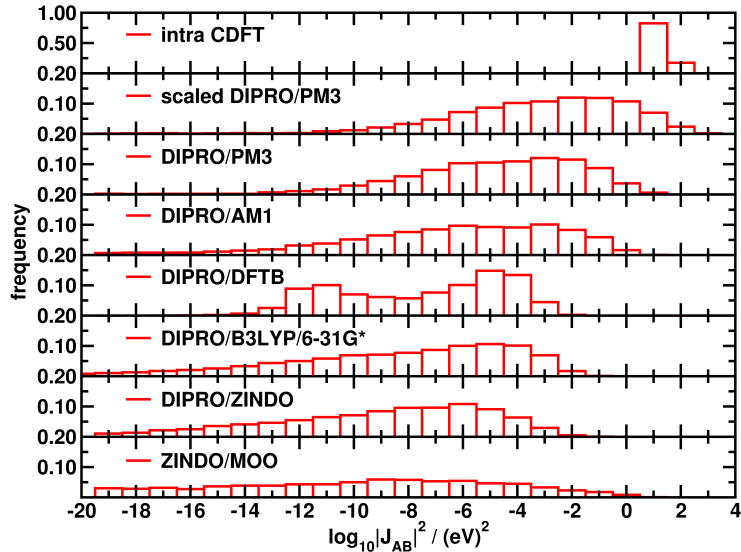


Figure 3.9: Distribution of the charge transfer integrals $\log_{10} |J_{AB}|^2$ for hole transfer in an amorphous, segmented P3HT morphology using ZINDO/MOO or DIPRO in conjunction with DFT/B3LYP/6-31G*, DFTB/3OB or semiempirical methods PM3, AM1, ZINDO.

3.1.4 Scaling the Charge Transfer Integral

The charge transfer integral $|J_{AB}|$ is evaluated using the DIPRO method in combination with different electronic structure methods for pairs of P3MT oligomers of variable length at different intermolecular distances and orientations, and compared to CDFT reference values. Thus, scaling factors are derived for the DIPRO approach in conjunction with DFT, PM3, ZINDO, DFTB/Mio-1-1, and DFTB/3OB-3-1 with respect to CDFT. So, we compare DFTB in two flavours using the Mio-1-1 parametrisation [256, 257] and the set of parameters of the third-order parametrisation for organic and biological systems (3OB-3-1) [258–260]. As CDFT is computationally rather demanding, we limit its application to small oligomers (i.e. 3mers, 5mers, and 7mers) of P3MT and pairs of DIPBI molecules.

The P3MT pairs are constructed from two planar molecules with various interplanar distances $\Delta z = [3.0, 3.5, 4.0, 5.0, 6.0] \text{ \AA}$ both at an initial position $\Delta x = 0.0 \text{ \AA}$ (see Fig. 3.10,i) and with a lateral shift about $\Delta x = 4.0 \text{ \AA}$ (Fig. 3.10,ii).

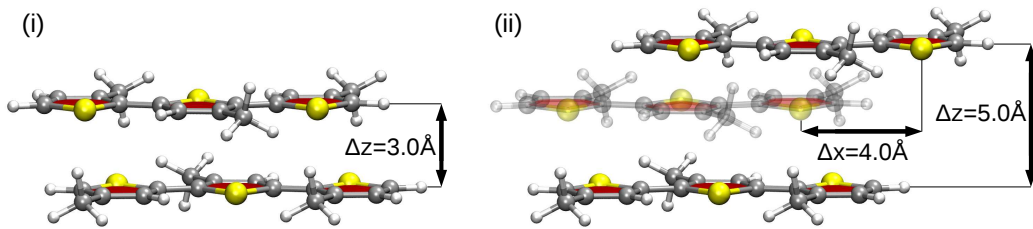


Figure 3.10: Relative alignment of a pair of P3MT 3mers without a lateral $\Delta x = 0 \text{ \AA}$ shift at a vertical distance $\Delta z = 3.0 \text{ \AA}$ (i) and a lateral shift $\Delta x = 4.0 \text{ \AA}$ and a vertical distance $\Delta z = 5.0 \text{ \AA}$ (ii).

As one can see in Figure 3.11, CDFT yields higher $|J_{AB}^h|$ values for hole transfer than the DIPRO approach for all configurations of P3MT pairs. A linear fit $|J_{AB}^h|_y = a|J_{AB}^h|_x + b$ was performed for each data set. Especially for low values of $|J_{AB}^h|$, the data is seen to lie close to the fitted line, while one observes larger deviations for larger $|J_{AB}^h|$ values. In the case of $|J_{AB}^h|_x$ DIPRO/PBE/6-311G** is scaled to $|J_{AB}^h|_y$ CDFT, the linear fit gives a slope of $a = 2.887$ and a y -axis intercept of $b = -32.01 \text{ meV}$ (Fig. 3.11,i). The application of a hybrid functional in the DIPRO calculations like B3LYP yields a reduction in the scaling factor to $a = [2.382, 2.389, 2.569]$ compared to DIPRO/PBE. Here, the charge transfer integral $|J_{AB}^h|$ shows a basis set dependence. One obtains a reduction of the $|J_{AB}^h|$ value with increasing basis set (B3LYP/3-21G*, B3LYP/6-31G*, B3LYP/6-311G**), which results in an increase of the scaling factor a (Fig. A.2,i,ii,iii). As it is not feasible to evaluate $|J_{AB}|$ for every hopping pair in the total morphology, one needs to apply a computational cheaper method like PM3, ZINDO or DFTB. If we scale $|J_{AB}^h|_x$ DIPRO/PM3 to $|J_{AB}^h|_y$ CDFT, we obtain $a = 6.886$ and a y -axis intercept of $b = -55.74 \text{ meV}$ (Fig. 3.11,ii). This factor a is larger than the scaling factor from DIPRO/PM3 to DIPRO/PBE/6-311G** with $a = 2.379$ (Fig. 3.11,iv). Scaling DIPRO data based on the semiempirical ZINDO to CDFT results yields a small scaling $a = 1.47$ and $b = 53.4 \text{ meV}$ (Fig. A.1,i). Comparing the DIPRO/DFTB parameterisations, we find a higher accordance of the 3OB-3-1 parametrisation with CDFT results ($R = 0.93$), with a slope $a = 3.48$ and a y -axis intercept of $b = 46.8 \text{ meV}$ (Fig. A.1,ii), than for Mio-1-1 ($R = 0.88$) using $a = 3.91$ and $b = 44.6 \text{ meV}$ (Fig. 3.11,iii). All linear fits for all different DIPRO variants are summarised in Table 3.2, the respective data sets are displayed in A.1.1 Figs. A.1,A.2,A.3,A.4.

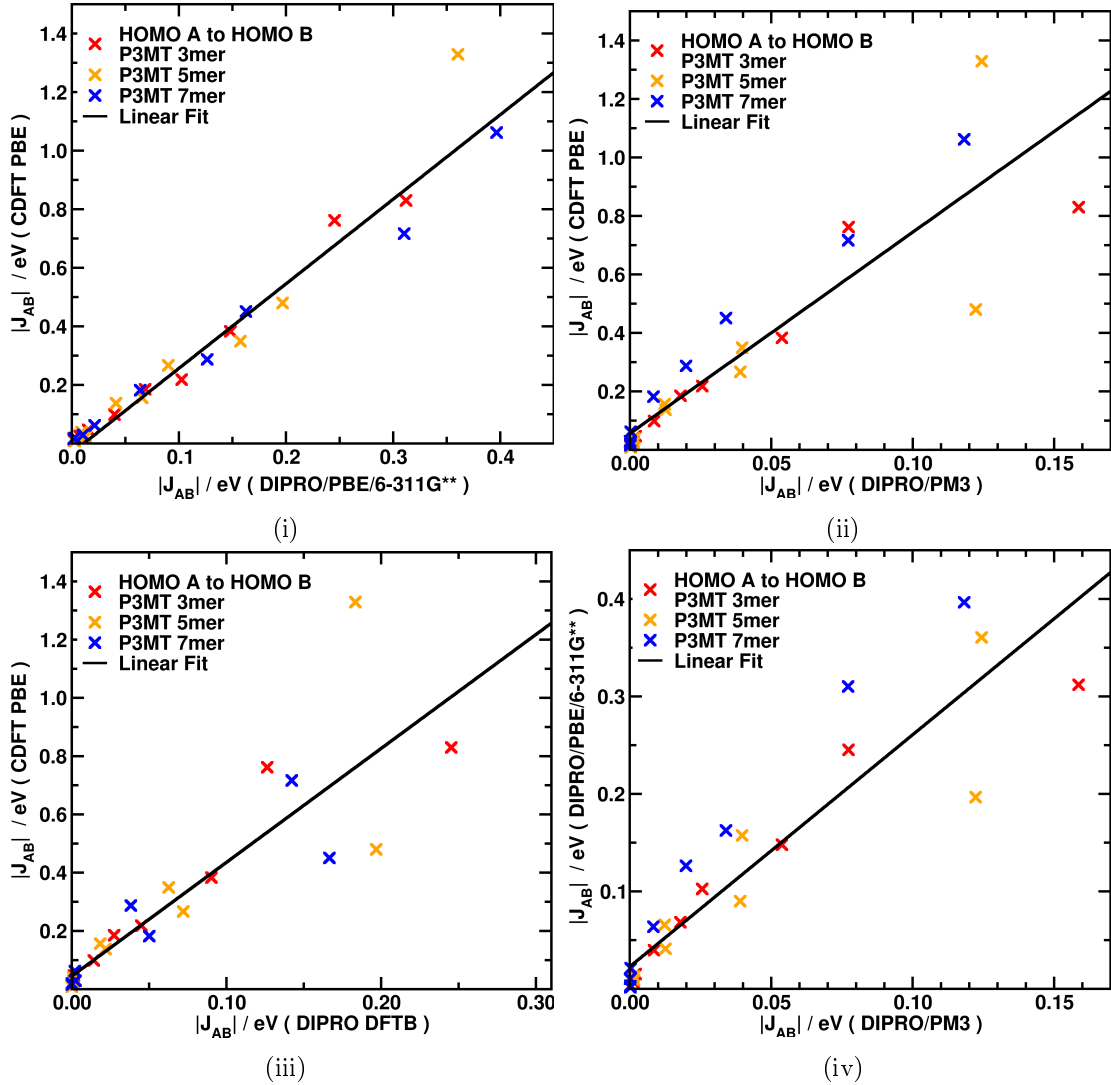


Figure 3.11: Charge transfer integral $|J_{AB}^h|$ for hole transfer in P3MT pairs of $n = [3, 5, 7]$. The DIPRO method in conjunction with (i) PBE/6-311G**, (ii) the semiempirical PM3, and DFTB/Mio-1-1 are scaled to CDFT/PBE/PW. (iv) DIPRO PM3 data is scaled to DIPRO/PBE/6-311G**. The P3MT pairs are generated as co-facial oriented, planar segments $\Delta x = 0 \text{ \AA}$ or with a lateral shift about $\Delta x = 4 \text{ \AA}$ for various distances $\Delta z = [3.0, 3.5, 4.0, 5.0, 6.0] \text{ \AA}$.

Table 3.2: Linear scaling for charge transfer integrals $|J_{AB}^h|$ for interchain hole transfer in P3MT. The linear fit $|J_{AB}|_y = a|J_{AB}^h|_x + b$ is applied. The P3MT pairs are generated as co-facial oriented, planar segments $\Delta x = 0 \text{ \AA}$ or with a lateral shift about $\Delta x = 4 \text{ \AA}$ for various distances $\Delta z = [3.0, 3.5, 4.0, 5.0, 6.0] \text{ \AA}$. The CDFT data is provided by Tobias Lettmann [75].

method $ J_{AB}^h _y$	method $ J_{AB}^h _x$	b [meV]	a	R
CDFT/PBE/PW	B3LYP/6-311G**	-9.87	2.569	0.973
CDFT/PBE/PW	B3LYP/6-31G*	-3.55	2.389	0.969
CDFT/PBE/PW	B3LYP/3-21G*	-6.20	2.446	0.969
CDFT/PBE/PW	PBE/6-311G**	-32.0	2.887	0.968
CDFT/PBE/PW	PM3	-55.7	6.886	0.908
CDFT/PBE/PW	ZINDO	53.4	1.474	0.936
CDFT/PBE/PW	DFTB/3OB-3-1	46.8	3.483	0.928
CDFT/PBE/PW	DFTB/Mio-1-1	44.6	3.910	0.881
PBE/6-311G**	DFTB/Mio-1-1	18.6	1.366	0.919
PBE/6-311G**	PM3	22.8	2.379	0.922
B3LYP/3-21G*	PM3	4.42	0.493	0.809
PM3	DFTB/Mio-1-1	-1.13	0.578	0.975

In a similar fashion the charge transfer integrals for electron transfer are summarised with a linear scaling behaviour $|J_{AB}^e|_y = a|J_{AB}^e|_x + b$ for various methods (Tab. 3.3). CDFT/PBE yields the highest $|J_{AB}^e|$ values for electron transfer.

Table 3.3: Linear scaling for charge transfer integrals $|J_{AB}^e|$ for intermolecular electron transfer in P3MT. The linear fit $|J_{AB}^e|_y = a|J_{AB}^e|_x + b$ is applied. The P3MT pairs are generated as co-facial oriented, planar segments $\Delta x = 0 \text{ \AA}$ or with a lateral shift about $\Delta x = 4 \text{ \AA}$ for various distances $\Delta z = [3.0, 3.5, 4.0, 5.0, 6.0] \text{ \AA}$.

method $ J_{AB}^e _y$	method $ J_{AB}^e _x$	b [meV]	a	R
CDFT/PBE/PW	B3LYP/6-311G**	50.7	1.839	0.955
CDFT/PBE/PW	B3LYP/6-31G*	76.8	1.717	0.951
CDFT/PBE/PW	B3LYP/3-21G*	80.7	1.785	0.948
CDFT/PBE/PW	PBE/6-311G**	32.4	2.251	0.973
CDFT/PBE/PW	PM3	127.1	5.439	0.955
CDFT/PBE/PW	ZINDO	96.8	1.589	0.961
CDFT/PBE/PW	DFTB/3OB-3-1	79.6	3.502	0.986
CDFT/PBE/PW	DFTB/Mio-1-1	81.3	3.104	0.975
PBE/6-311G**	DFTB/Mio-1-1	24.6	1.354	0.984
PBE/6-311G**	PM3	40.2	2.429	0.986
B3LYP/3-21G*	PM3	28.9	2.975	0.984
PM3	DFTB/Mio-1-1	-4.29	0.539	0.965

The $|J_{AB}^e|$ CDFT/PBE are approximated linearly by means of DIPRO/PBE/6-311G** calculations with a scaling factor $a = 2.251$ at a y-intercept of $b = 50.7 \text{ meV}$ (Fig. 3.12,i). The fit yields the highest correlation coefficient $R = 0.973$ to reproduce CDFT data in the selection of methods discussed here.

If we compare DIPRO/B3LYP in conjugation with the basis sets 6-311G**/6-31G*/3-21G* to CDFT/PBE, we obtain a similar reduction for electrons in the scaling factors $a = [1.839, 1.717, 1.785]$ as found for holes (Fig. A.5,i,ii,iii). An increasing basis set leads to a higher correlation coefficient R for the linear fits. The scaling factors a from DIPRO/DFT to CDFT are smaller for electron transfer than for hole transfer. The DIPRO PM3 approach yields the highest scaling factor $a = 5.439$ to CDFT (Fig. 3.12,ii), whereas we obtain $a = 3.104$ for DIPRO/DFTB/Mio-1-1 (Fig. 3.12,iii) and $a = 3.502$ for DFTB/3OB-3-1 (Fig. 3.12,iv), which both exceed the values for DIPRO/DFT-based data. All respective data sets for electron transfer integrals and linear regressions are displayed in Figs. A.5,A.6.

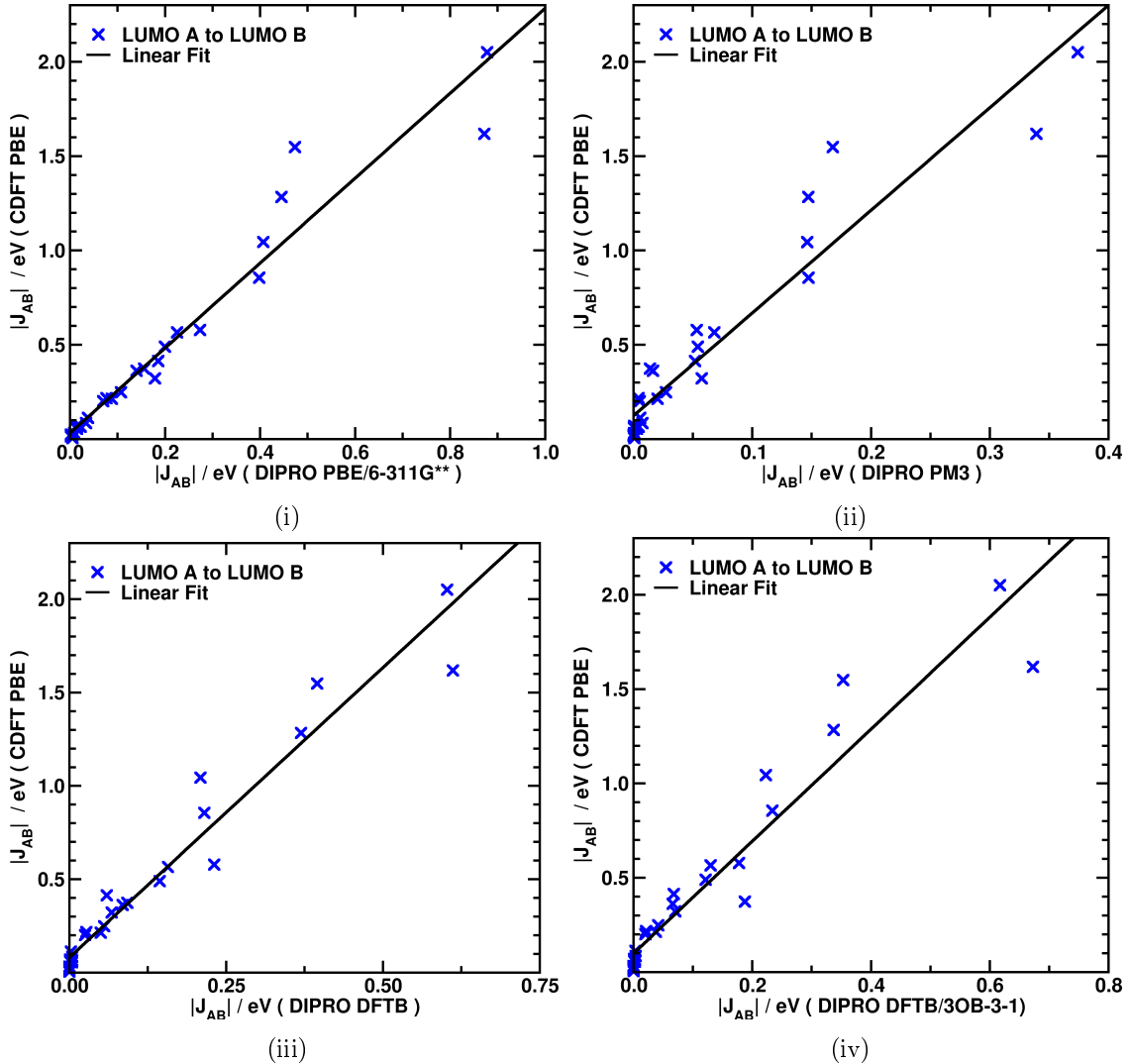


Figure 3.12: Charge transfer integral $|J_{AB}^e|$ for electron transfer between P3MT dimer structures with thiophene segment length $n = [3, 5, 7]$. The DIPRO data with electronic structure methods (i) PBE/6-311G**, (ii) semi-empirical PM3, (iii) DFTB/Mio-1-1, and (iv) DFTB/3OB-3-1 are compared to the CDFT/PBE/PW. The P3MT pairs are generated as co-facial oriented, planar segments $\Delta x = 0 \text{ \AA}$ or with a lateral shift about $\Delta x = 4 \text{ \AA}$ for various distances $\Delta z = [3.0, 3.5, 4.0, 5.0, 6.0] \text{ \AA}$.

When using linear scaling on $|J_{AB}|$, the question arises whether the $|J_{AB}|$ with a semiempirical method such as PM3 achieves sufficient accuracy at all, if not only idealised example geometries are considered but pairs from the atomistic morphology. When we compare the $|J_{AB}|$ for hole transfer for DIPRO/PM3 with those from B3LYP/6-31G* for pairs within the entire morphology, we obtain a wide scatter of the calculated results. Both methods can have deviations of more than two orders of magnitude in the data (Fig. 3.13). Nevertheless, in consideration of the significantly higher computational effort with approx. 120 times longer computational time for DIPRO/DFT compared to PM3, it is necessary to limit oneself to the scaling of the semiempirical methods.

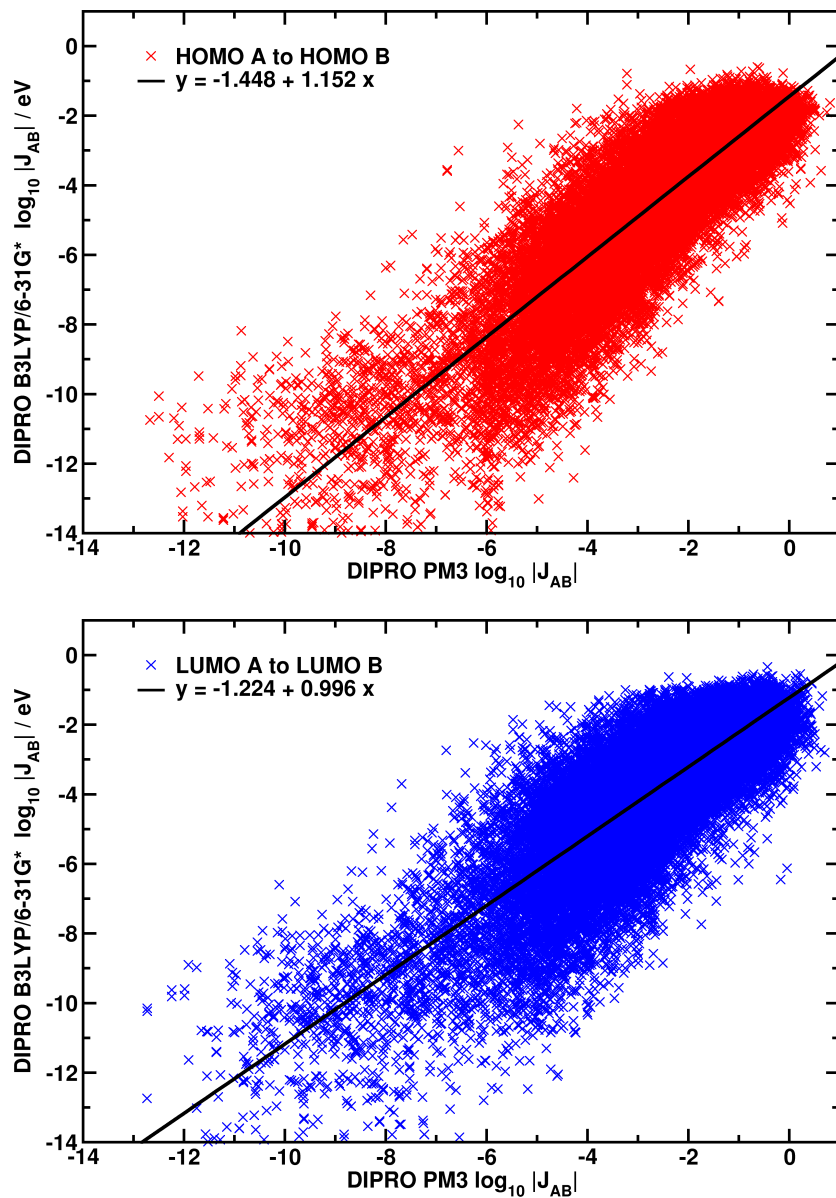


Figure 3.13: The DIPRO/B3LYP/6-31G* charge transfer integral $\log_{10} |J_{AB}|$ for hole (red) and electron transfer (blue) as a function of DIPRO/PM3. The plot includes the data for pairs for the 12 nearest neighbours of every hopping site in the P3HT:DIPBI morphology.

3.1.5 Geometric Parametrisation

An alternative approach to $|J_{AB}|$ for a high number of pairs in the P3HT:DIPBI morphology is the application of a fitting schema based on geometrically obtained parameters. Therefore, all charge transfer integrals are evaluated using the DIPRO/PM3 approach for dimer pairs in the nearest neighbour list, including the twelve nearest neighbours.

We introduce three quantities for determining the distance between two molecules d . The minimal appearing distance (MA) between two atoms of both molecules in the dimer configuration is labelled as d_{MA} , the mean minimal appearing distance d_{MMA} and the centre of mass distances d_{COM} after adding the hydrogen atoms in case of going from the atomistic united atom representation to a QM representation. The distances are defined for a dimer consisting of two monomers A and B with a number of N_A nuclear coordinates $\mathbf{R}_i \in \{\mathbf{R}_A\}$ and N_B in $\mathbf{R}_j \in \{\mathbf{R}_B\}$ and the total masses M_A and M_B , respectively.

$$d_{MA} = \min|\mathbf{R}_i - \mathbf{R}_j| \quad (273)$$

$$d_{MMA} = \frac{1}{N_A} \sum_{i=1}^{N_A} \min|\mathbf{R}_i - \mathbf{R}_j| \quad (274)$$

$$d_{COM} = \left| \frac{1}{M_A} \sum_{i=1}^{N_A} M_i \mathbf{R}_i - \frac{1}{M_B} \sum_{j=1}^{N_B} M_j \mathbf{R}_j \right| \quad (275)$$

All three distance measures can be obtained from the nuclear coordinate configuration, but they lack detailed information about the relative orientation of the molecules. The minimal appearing distance d_{MA} only refers to one single pair of atoms and does not hold information about other atoms in the charge-transfer complex. This deficiency is attenuated in part by d_{MMA} . The distance between two centres of mass d_{COM} of two molecules can be far off, even if some parts of a molecule are close to each other. For long polymer chains with kinks and bendings, the centre of mass can be located even outside the polymer chain, and in this case, d_{COM} provides only limited information about the actual situation of the charge transfer process. We introduce a further measure called the ring centre of mass distance d_{RCOM} (Eq. 280), which refers to the centre of the thiophene unit plains in the P3HT polymer backbone chain, leading to an improved description for the distance between conjugated π -systems of two aligned molecules.

We plot the DIPRO/PM3-based $\log_{10}|J_{AB}^h|$ for the HOMO A to HOMO B transitions as a function of the distance measures $d_x \in [d_{MA}, d_{MMA}, d_{COM}]$ for pairs from the morphology at 500 K (Fig. 3.14). Analogously, we consider $|J_{AB}^e|$ as a LUMO A to LUMO B transition for electron transfer.

We find similar structuring in the distribution of transfer integrals for holes and electrons. We see the tendency for $|J_{AB}|$ to drop sharply with increasing distance d_x in the logarithmic plots, indicating the exponential decay of $|J_{AB}|$ as a function of d_x . Both $|J_{AB}^h|$ and $|J_{AB}^e|$ scatter very strongly by up to seven orders of magnitude for fixed d_x . We find two accumulation spots of $|J_{AB}^h|$ depending on d_{MA} in the range of 1.7 Å to 3.2 Å and 4.8 Å to 6.4 Å. Whereas, only a single broadened accumulation cluster results for d_{MMA} and d_{COM} , respectively.

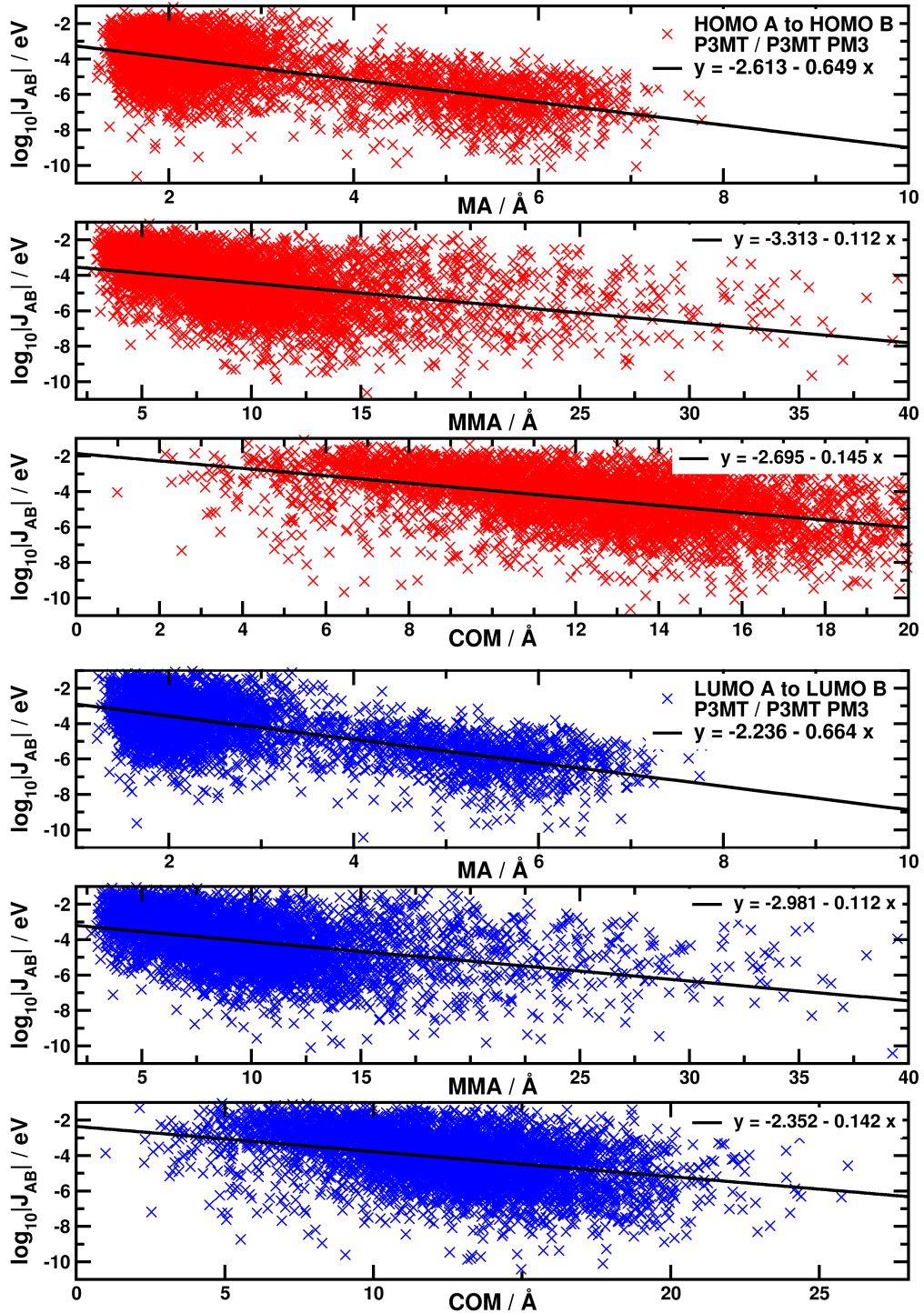


Figure 3.14: A geometric parametrisation of the charge transfer integral $\log_{10} |J_{AB}|$ between P3MT/P3MT dimers with DIPRO/PM3 for hole transfer as a HOMO A to HOMO B transition (red) and for electron transfer DIPRO/PM3 as a LUMO A to LUMO B transition (blue) as a function of the minimal appearing distance (MA) d_{MA} , the mean minimal appearing distance d_{MMA} and the centre of mass distances d_{COM} . The P3MT/P3MT dimers are extracted from the morphology at 500 K.

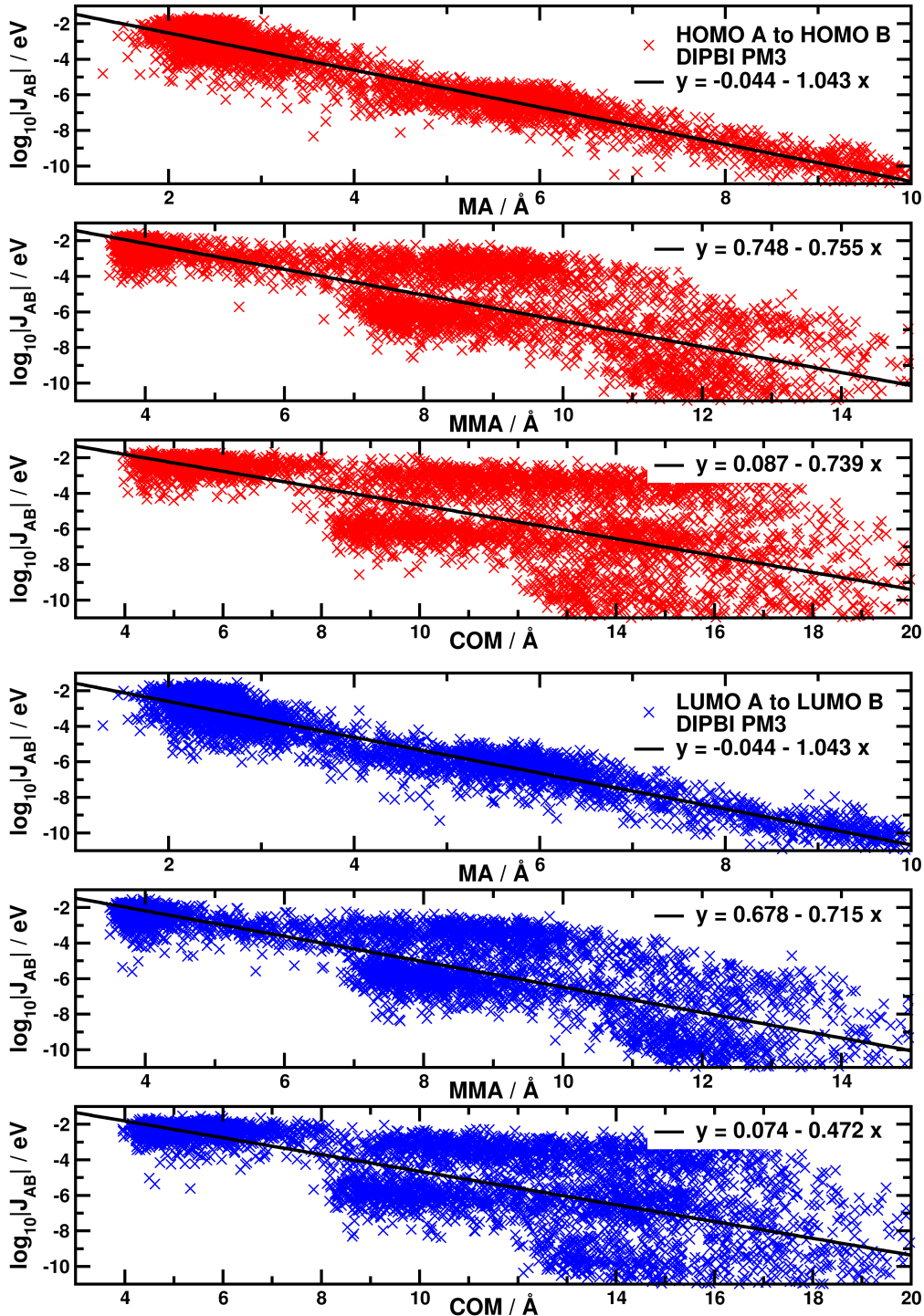


Figure 3.15: A geometric parametrisation of the charge transfer integral $\log_{10} |J_{AB}|$ between DIPBI/DIPBI dimers with DIPRO/PM3 for hole transfer as a HOMO A to HOMO B transition (red) and for electron transfer DIPRO/PM3 as a LUMO A to LUMO B transition (blue) as a function of the minimal appearing distance (d_{MA}) d_{MA} , the mean minimal appearing distance d_{MMA} and the centre of mass distances d_{COM} . The DIPBI/DIPBI dimers are extracted from the morphology at 500 K. The parametrisation of the data with d_{MA} shows the best correlation coefficient in the selected set of parameters d_{MA} , d_{MMA} or d_{COM} for the parametrisation of the data.

There is also a fair amount of scattering in the plot $|J_{AB}|$ versus d_{MA} , d_{MMA} and d_{COM} , shown in Fig. 3.15. The best linearly approximable distribution is obtained for DIPBI/DIPBI pairs with d_{MA} . The data reveals three accumulation points at $d_{MA} = [2.0 - 3.8] \text{ \AA}$, and $d_{MA} = [5.0 - 6.5] \text{ \AA}$ and $d_{MA} = [8.5 - 10.5] \text{ \AA}$. They correspond to DIPBI/DIPBI pairs with the first, second and third nearest neighbours in π -stacks. A similar characterisation into three groups can also be made for d_{MMA} and d_{COM} in DIPBI/DIPBI. However, there is also a group of pairs with elevated $|J_{AB}|$ for intermediate distances $d_{COM} = [5 - 10] \text{ \AA}$.

We have linearly approximated the $\log_{10}|J_{AB}|$ in the distributions to obtain a general, geometric parametrisation of the charge transfer integrals for the distances d_{MA} , d_{MMA} and d_{COM} . The linear fit parameters for the hole transfer integrals $|J_{AB}^h|$ are summarised in Table 3.4 using a linear scaling $\log_{10}|J_{AB}|_y = a \cdot d_x + b$ for a single quantity or a linear combination of these three geometric quantities $f(d_{MA}, d_{MMA}, d_{COM}) = \log_{10}|J_{AB}| = A \cdot d_{MA} + B \cdot d_{MMA} + C \cdot d_{COM} + D$. R denotes the correlation coefficient. Similarly, the linear fit parameters are shown in Table 3.5 for the charge transfer integrals of electrons $|J_{AB}^e|$ as LUMO A to LUMO B transitions. The underlying data for the fits in the Tables 3.4 and 3.5 is displayed for P3MT/P3MT dimers in Figure 3.14, for hetero-molecular dimers of DIPBI/P3MT in A.8 and DIPBI/DIPBI dimers in 3.15.

The best correlation for the linear fit is found for the DIPBI/DIPBI data as a function of d_{MA} with $R = 0.968$. The majority of the scaling schemas result in a small correlation coefficient $R < 0.7$, as the $|J_{AB}|$ values can spread more than two orders of magnitude for distinct orientation of molecules with similar geometric parameters d_x . In general, the parametrisation via d_{MA} results in a higher correlation coefficient R than d_{MMA} and is even better than the centre of mass distance d_{COM} . The use of a linear combination $f(d_{MA}, d_{MMA}, d_{COM})$ improves the parameterisation for P3MT/P3MT and P3MT/DIPBI transitions as reflected in the enhanced correlation coefficients $R = 0.659$ and $R = 0.672$, respectively. The optimised parameters of f are listed in Table 3.4. Nevertheless, it can be seen from the enormous scatter of the values f that the chosen geometric parameters are not sufficient to reproduce $|J_{AB}|$ with adequate accuracy (Fig. A.9).

Due to small correlation coefficients, the geometric parametrisation method is only applied as a backup-method to determine $|J_{AB}|$ if the electronic structure calculations for DIPRO fail to convergence for a pair of adjacent molecules in the morphology.

A further approach to parametrise the $|J_{AB}|$ for a pair of DIPBI/DIPBI molecules is obtained when taking the relative orientation angle ϑ of both normal vectors \mathbf{n}_i to the DIPBI molecule plain into account (see Sec. A.1.7). The distribution of $|J_{AB}|$ as a function of ϑ and the distances d_{MA} , d_{MMA} and d_{COM} is displayed in Fig. 3.16 and A.7. The values for $|J_{AB}|$ are presented in a colour-coded schema and can vary various orders of magnitude. The highest $|J_{AB}|$ values are obtained for pairs with a small minimal distance d_{MA} and a low angle $\vartheta \in [0^\circ, 30^\circ]$. But nevertheless, dimers in a non- π -stacking orientation or even in an orthogonal configurations with a $\vartheta \in [40^\circ, 90^\circ]$ can yield $|J_{AB}| \geq 1.0 \times 10^{-3} \text{ eV}$, if the minimal distance is low $d_{MA} \in [1.8, 3.5] \text{ \AA}$. d_{MMA} provides the highest resolution for the discrimination of the stacking level (Fig. A.7). Also these plots (Fig. 3.16) suggest that d_{MA} discriminates the $|J_{AB}|$ best in the selected set of geometric quantities d_{MA} , d_{MMA} , d_{COM} , ϑ .

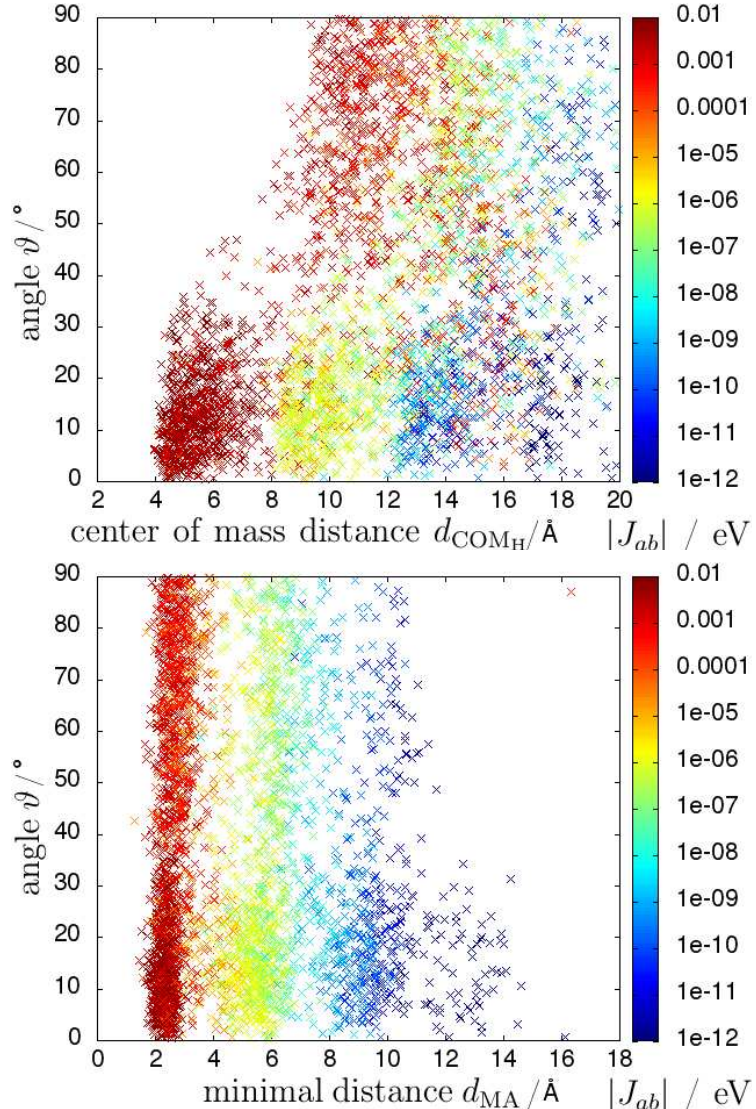


Figure 3.16: The charge transfer integral $|J_{AB}|$ between DIPBI/DIPBI dimers with the DIPRO/PM3 approach for hole transfer as a HOMO A to HOMO B transition as a function of the angle $\vartheta \in [0^\circ, 90^\circ]$ and the minimal distance d_{MA} , the mean minimal distance d_{MMA} and the centre of mass distance d_{COM} . The values for $|J_{AB}|/\text{eV}$ are presented in a colour-coded schema and vary various orders of magnitude. The data displays 3752 DIPBI/DIPBI in the P3HT:DIPBI morphology at 500 K.

Some attempts to use neural networks and deep learning algorithms (TensorFlow [283]) to determine DIPRO/PM3-based $|J_{AB}|$ as a function of the nuclear coordinate configuration, geometric parameters, or the inertia tensor and the corresponding principal moments of inertia did not yield results with adequate accuracy. The neural network trained with 6×10^4 data sets of charge transfer pairs yields values for $|J_{AB}|$ that are two to four orders of magnitude different from DIPRO data. This suggests that the size of the data set is not sufficient to provide an adequate alternative for determining $|J_{AB}|$. Using geometric distance measures as input provides higher accuracy for $|J_{AB}|$ than nuclear coordinates.

Table 3.4: A geometric parametrisation of the charge transfer integral for hole transfer DIPRO/PM3 as a HOMO A to HOMO B transition as a function of the minimal appearing distance (MA) d_{MA} , the mean minimal appearing distance d_{MMA} and the centre of mass distances d_{COM} . The following parametrisation uses P3MT/P3MT, P3MT/DIPBI and DIPBI/DIPBI dimers from the morphology at 500 K. The linear fits are determined as $\log_{10} |J_{AB}|_y = a \cdot d_x + b$ or as a linear combination $f(d_{\text{MA}}, d_{\text{MMA}}, d_{\text{COM}}) = \log_{10} |J_{AB}| = A \cdot d_{\text{MA}} + B \cdot d_{\text{MMA}} + C \cdot d_{\text{COM}} + D$. R is the correlation coefficient.

molecule pair	parameter	function / coefficients	R
P3MT / P3MT	d_{MA}	y = -2.613-0.649·x	0.617
P3MT / P3MT	d_{MMA}	y = -3.313-0.112·x	0.422
P3MT / P3MT	d_{COM}	y = -2.649-0.145·x	0.464
P3MT / P3MT	$d_{\text{MA}}, d_{\text{MMA}}, d_{\text{COM}}$	$A = -0.108; B = -0.575$ $C = 7.636\text{E}-4; D = -1.503$	0.659
P3MT / DIPBI	d_{MA}	y = -2.942-0.847·x	0.536
P3MT / DIPBI	d_{MMA}	y = 2.377-0.386·x	0.429
P3MT / DIPBI	d_{COM}	y = -4.298-0.054·x	0.278
P3MT / DIPBI	$d_{\text{MA}}, d_{\text{MMA}}, d_{\text{COM}}$	$A = -0.432; B = -0.168$ $C = -0.039; D = -2.223$	0.672
DIPBI / DIPBI	d_{MA}	y = -0.435-1.043·x	0.968
DIPBI / DIPBI	d_{MMA}	y = 0.748-0.755·x	0.824
DIPBI / DIPBI	d_{COM}	y = 0.087-0.739·x	0.679

Table 3.5: A geometric parametrisation of the charge transfer integral for electron transfer DIPRO/PM3 as a LUMO A to LUMO B transition as a function of the minimal appearing distance (MA) d_{MA} , the mean minimal appearing distance d_{MMA} and the centre of mass distances d_{COM} . The following parametrisation uses P3HT/P3HT, P3HT/DIPBI and DIPBI/DIPBI dimers from the morphology at 500 K. The linear fits are determined as $\log_{10} |J_{AB}|_y = a \cdot d_x + b$. R is the correlation coefficient.

molecule pair	parameter	function	R
P3MT / P3MT	d_{MA}	y = -2.236-0.664·x	0.627
P3MT / P3MT	d_{MMA}	y = -2.981-0.112·x	0.452
P3MT / P3MT	d_{COM}	y = -2.352-0.142·x	0.439
P3MT / DIPBI	d_{MA}	y = -2.758-0.823·x	0.551
P3MT / DIPBI	d_{MMA}	y = -2.156-0.382·x	0.448
P3MT / DIPBI	d_{COM}	y = -3.957-0.057·x	0.313
DIPBI / DIPBI	d_{MA}	y = -0.578-1.009·x	0.964
DIPBI / DIPBI	d_{MMA}	y = 0.678-0.715·x	0.836
DIPBI / DIPBI	d_{COM}	y = 0.074-0.472·x	0.695

3.1.6 Parametrisation as a Function of the Overlap Integral

An alternative approach to determine the charge transfer integral $|J_{AB}|$ is the parametrisation as a function of the intermolecular overlap integral $|S_{AB}|$ between the frontier molecular orbitals of both monomers in the charge transfer dimer configuration. This offers the advantage that the determination of $|S_{AB}|$ is usually less computationally intensive than that of $|J_{AB}|$. In general, we determine the overlap integral $|S_{AB}^h|$ for hole transfer as a HOMO A to HOMO B transition and electron transfer $|S_{AB}^e|$ as a LUMO A to LUMO B transition.

In a double logarithmic plot, one can find a correlation between $|J_{AB}|^2$ and $|S_{AB}|$ (Fig. 3.17). The density plot displays the $\log_{10} |J_{AB}|^2$ for $\approx 4 \times 10^5$ charge transfer pairs from 12 distinct P3HT:DIPBI morphology frames. One can see that $\log_{10} |J_{AB}|^2$ roughly increases with $\log_{10} |S_{AB}|$, even though the values spread several orders of magnitude (Fig. 3.17). The plot shows an ascending distribution with a centered accumulation band. Especially, we see a high density of pairs with an overlap in the range of $\log_{10} |S_{AB}| = [-5, -3]$ with $\log_{10} |J_{AB}|^2$ in the range of $[-3, -1] \text{ eV}^2$. The $|S_{AB}|$ data, which is smaller than $\log_{10} |S_{AB}| = -14$, samples numeric noise without any physical overlap at long intermolecular distances.

In analogy we can find a similar dependence of the transfer integral for electron transfer $|J_{AB}^e|$ on the overlap $|S_{AB}^e|$ (Fig. A.10).

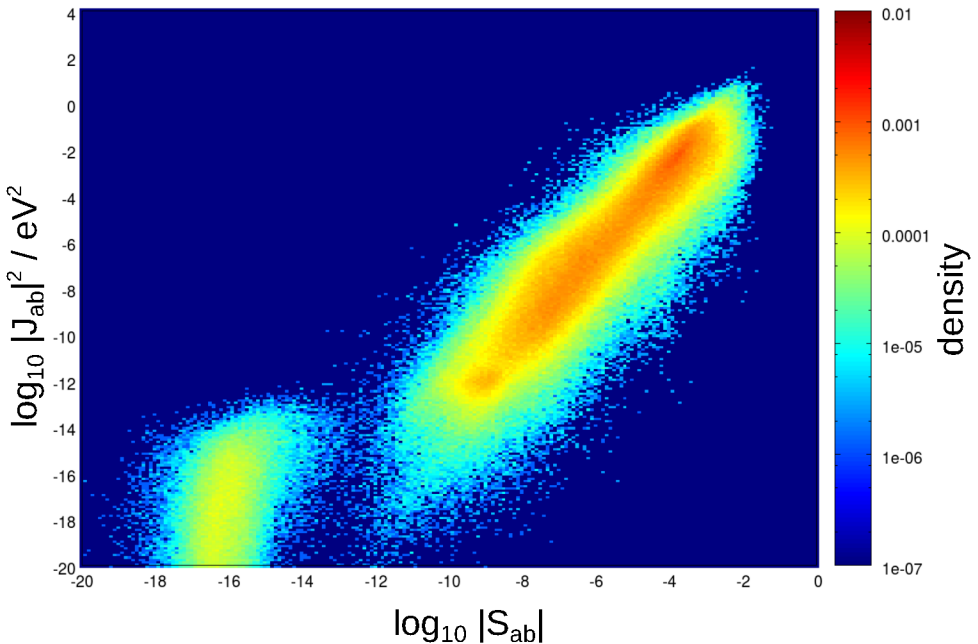


Figure 3.17: Density plot of the charge transfer integral $\log_{10} |J_{AB}|^2$ for hole transfer (DIPRO/PM3) as a function of the overlap $\log_{10} |S_{AB}|$ for neighbouring $\approx 4 \times 10^5$ charge transfer pairs in 12 frames in P3HT:DIPBI morphologies.

One can approximate the ascending $\log_{10} |J_{AB}|$ linearly as a function of $|S_{AB}|$ using $\log_{10} |J_{AB}| = a \log_{10} |S_{AB}|$. Even though the values spread three orders of magnitude, we can use this linear fit to estimate the charge transfer integral based on the evaluated overlap integral. This finding also holds, if we treat P3MT without invoking a segment partitioning scheme ($n = 32$) and evaluate $|J_{AB}|$ and $|S_{AB}|$ for pairs in the 6 nearest neighbours list and a minimal distance in the range $d_{MA} = [1.0, 6.0] \text{ \AA}$ (Fig. 3.18).

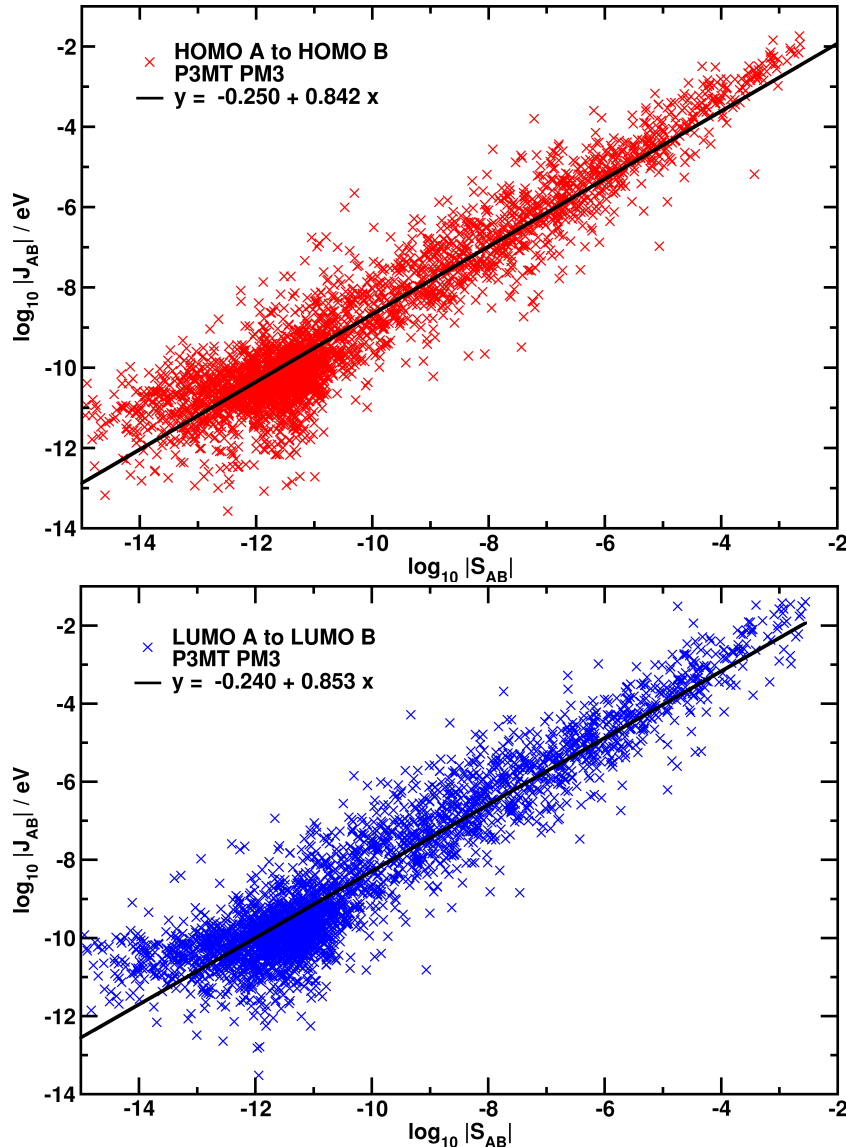


Figure 3.18: The charge transfer integral $\log_{10} |J_{AB}|$ for hole (red) and electron transfer (blue) with DIPRO/PM3 as a function of the overlap $\log_{10} |S_{AB}|$ for transfer between P3MT $n = 32$ chains for the 6 nearest neighbours in the P3HT:DIPBI morphology. The 3000 selected pairs possess a minimal distance in the range $d_{MA} = [1.0, 6.0]\text{\AA}$. In the double logarithmic plot, we approximate the ascending $\log_{10} |J_{AB}|$ linearly $\log_{10} |J_{AB}| = a \log_{10} |S_{AB}| + b$ with $a = 0.842$ and $b = -0.250$ (hole) and $a = 0.853$ and $b = -0.240$ (electron).

The initial idea is to apply a computationally cheap, semiempirical method to evaluate $|S_{AB}|$ with a reasonable accuracy and use a scaling method to mimic results for $|S_{AB}|$ and $|J_{AB}|$ from high-level, sophisticated, computational expensive methods like DFT or CDFT for a test set of dimer configurations (Fig. 3.19). In a second step these scaling methods can be exploited to determine $|J_{AB}|$ for a high number of pairs amount $N^{\text{pairs}} \approx 5 \times 10^5$ per frame in the entire P3HT:DIPBI morphology. Thus, we make the methodology applicable to a higher number of morphological frames. We apply the overlap of the CDFT-based diabatic wavefunctions as the standard method for $|S_{AB}|$ calibration.

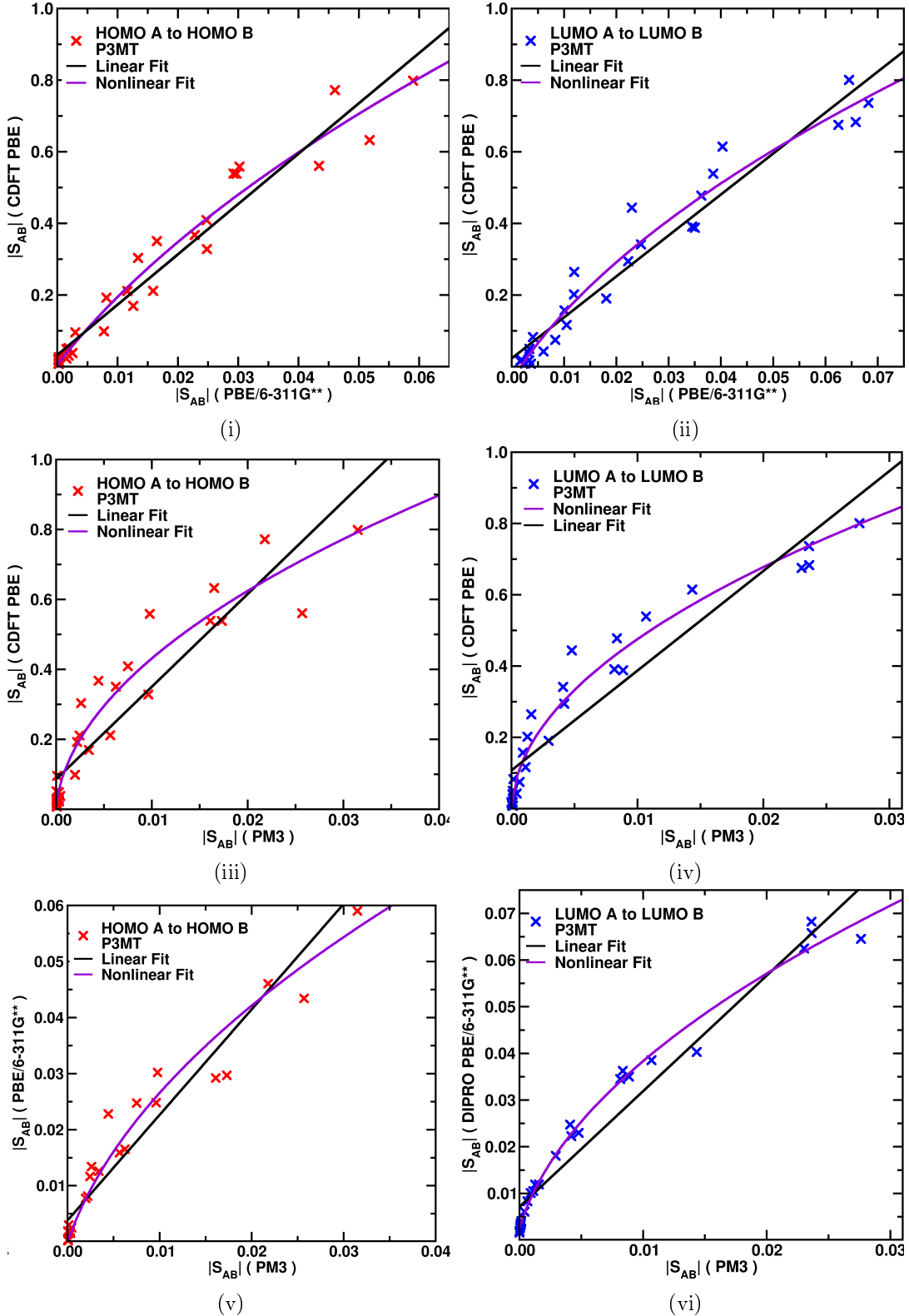


Figure 3.19: The overlap integral for hole $|S_{AB}^h|$ (red) and electron transfer $|S_{AB}^e|$ (blue) in P3MT $n = [3, 5, 7]$. The overlap integrals are scaled for PBE/6-311G** (i, ii) and PM3 (iii, iv) to CDFPBE, and the PM3 method (v, vi) is scaled to PBE/6-311G**. The P3MT dimers are generated as planar segments with various distances $[3.0, 3.5, 4.0, 5.0, 6.0] \text{ \AA}$ or with 3.0 \AA and a lateral shift about 4 \AA . Linear and nonlinear fits are displayed for parametrisation.

The linear parametrisation $|S_{AB}|_y = a|S_{AB}|_x + b$ and nonlinear parametrisation $|S_{AB}|_y = \sqrt{A1|S_{AB}|_x + A2} + A3$ as a correlation between different electronic structure methods are listed in Table 3.6. The application of a nonlinear fit function results in higher correlation coefficients R than in the linear case. The linear scaling factors a for DFT-based results are in a similar range from $a = 13.5$ to 15.0 . An increase in the applied basis set B3LYP/3-21G*/6-31G*/6-311G** (Fig. A.11,i,ii,iii) yields higher correlation coefficients R . The overlap from PM3 is the smallest in the data (Fig. 3.19,v). DFTB/Mio-1-1 (Fig. A.11,iv,v,vi) does not achieve the quality of CDFT or DFT results but gives higher values than the semiempirical PM3 method.

Table 3.6: A parametrisation of the intermolecular frontier orbital overlap $|S_{AB}|$ in P3MT for hole transfer in a HOMO A to HOMO B transition. P3MT dimer structures with distinct chain length $n = [3, 5, 7]$ are applied in the parametrisation. CDFT results are compared to DFT with PBE/6-311G**, B3LYP/6-311G**/6-31G*/3-21G* or PM3, DFTB/MIO-1-1. Linear fits $|S_{AB}|_y = a|S_{AB}|_x + b$ and nonlinear fits are applied $|S_{AB}|_y = \sqrt{A1|S_{AB}|_x + A2} + A3$. The CDFT data is provided by Tobias Lettmann [75].

Linear fit					
method $ S_{AB} _y$	method $ S_{AB} _x$	a	b		R
CDFT/PBE PW	PBE/6-311G**	14.053	0.0325		0.972
CDFT/PBE PW	B3LYP/6-311G**	13.517	0.0336		0.970
CDFT/PBE PW	B3LYP/6-31G*	15.006	0.0499		0.969
CDFT/PBE PW	B3LYP/3-21G*	14.506	0.0592		0.966
CDFT/PBE PW	DFTB	16.873	0.0789		0.944
CDFT/PBE PW	PM3	26.472	0.0858		0.923
CDFT/PBE PW	ZINDO	77.774	0.0679		0.952
CDFT/PBE PW	DFTB/3OB-3-1	70.147	0.1289		0.808
PBE/6-311G**	PM3	1.882	0.0038		0.949
PBE/6-311G**	DFTB	1.202	0.0033		0.971
PM3	DFTB	0.664	-0.0091		0.991
Nonlinear fit					
method $ S_{AB} _y$	method $ S_{AB} _x$	A1	A2	A3	R
CDFT/PBE PW	PBE/6-311G**	28.507	0.430	-0.639	0.979
CDFT/PBE PW	B3LYP/6-311G**	25.298	0.346	-0.583	0.978
CDFT/PBE PW	B3LYP/6-31G*	24.893	0.223	-0.460	0.982
CDFT/PBE PW	B3LYP/3-21G*	23.367	0.204	-0.425	0.986
CDFT/PBE PW	DFTB	15.729	0.012	-0.092	0.978
CDFT/PBE PW	PM3	21.876	2.6E-3	-0.039	0.965
CDFT/PBE PW	ZINDO	17.183	17.5E-3	-0.118	0.977
CDFT/PBE PW	DFTB/3OB-3-1	60.55	1.2E-3	-0.038	0.937
PBE/6-311G**	PM3	0.158	2.7E-4	-0.0165	0.969
PBE/6-311G**	DFTB	0.119	6.17E-4	-0.024	0.985
PM3	DFTB	0.117	6.72E-3	-0.0824	0.988

In a similar fashion the intermolecular frontier orbital overlap $|S_{AB}|$ in P3MT for electron transfer for a LUMO A to LUMO B transition are summarised for various scaling methods (Tab. 3.7). The electron data is determined for the same P3MT dimer configurations [3mer, 5mer, 7mer] with different distances as the reference data for hole transfer.

In general, the electron data requires smaller scaling factors a for DFT results to adjust to CDFT/PBE data than the corresponding hole data, e.g. for PBE/6-311G** $a^h = 14.05$ (Tab. 3.6) and $a^e = 11.43$ (Tab. 3.7). Fitting the orbital overlap $|S_{AB}|$ for electron transfer via a nonlinear fit instead of a linear scaling method yields higher correlation coefficients R (Tab. 3.7). In particular, B3LYP/6-311G** provides the highest value $R = 0.98$ to reproduce the CDFT-based data.

Furthermore, the CDFT results are compared to DFT/PBE/6-311G** (Fig. 3.19,ii) and PM3, where the DFT data yields a better agreement with the CDFT data than the PM3 method (Fig. 3.19,vi). The basis set dependence for electron transfer with DFT/B3LYP/6-311G**/6-31G*/3-21G* and scaling to CDFT is displayed in Figure (A.12,i,ii,iii). Reducing the size of the base set does not significantly reduce the accuracy represented by a constant R . The comparison of DFTB/Mio-1-1 to CDFT, PBE/6-311G** and PM3 is summarised in Figure (A.12,iv,v,vi).

Table 3.7: Parametrisation of the intermolecular frontier orbital overlap $|S_{AB}|$ in P3MT for electron transfer in a LUMO A to LUMO B transition. P3MT dimer structures with distinct segment length $n = [3, 5, 7]$ are applied in the parametrisation. CDFT results are compared to DFT with PBE/6-311G**, B3LYP/6-311G**/6-31G*/3-21G* or PM3, DFTB/MIO-1-1. Linear fits $|S_{AB}|_y = a|S_{AB}|_x + b$ and nonlinear fits are applied $|S_{AB}|_y = \sqrt{A1|S_{AB}|_x + A2 + A3}$.

Linear fit					
method $ S_{AB} _y$	method $ S_{AB} _x$	a	b		R
CDFT/PBE PW	PBE/6-311G**	11.430	0.0232		0.971
CDFT/PBE PW	B3LYP/6-311G**	10.687	0.0179		0.978
CDFT/PBE PW	B3LYP/6-31G*	11.677	0.0739		0.962
CDFT/PBE PW	B3LYP/3-21G*	11.827	0.0919		0.950
CDFT/PBE PW	DFTB	21.214	0.1052		0.946
CDFT/PBE PW	PM3	27.979	0.1071		0.937
CDFT/PBE PW	ZINDO	14.415	0.1219		0.916
CDFT/PBE PW	DFTB/3OB-3-1	37.683	0.1736		0.899
PBE/6-311G**	PM3	2.476	7.155E-3		0.976
PBE/6-311G**	DFTB	1.851	7.250E-3		0.972
PM3	DFTB	0.7448	4.537E-5		0.992
Nonlinear fit					
method $ S_{AB} _y$	method $ S_{AB} _x$	A1	A2	A3	R
CDFT/PBE PW	PBE/6-311G**	18.126	0.147	-0.423	0.975
CDFT/PBE PW	B3LYP/6-311G**	10.248	7.264E-3	-0.179	0.983
CDFT/PBE PW	B3LYP/6-31G*	8.644	1.334E-3	-0.0456	0.982
CDFT/PBE PW	B3LYP/3-21G*	8.306	8.459E-3	-0.0146	0.980
CDFT/PBE PW	DFTB	20.188	9.360E-3	-0.0595	0.977
CDFT/PBE PW	PM3	23.861	0.497E-3	-0.0137	0.969
CDFT/PBE PW	ZINDO	12.813	1.124E-3	-0.649E-3	0.976
CDFT/PBE PW	DFTB/3OB-3-1	30.105	2.128E-9	-9.680E-3	0.896
PBE/6-311G**	PM3	0.215	0.148E-3	-9.637E-3	0.996
PBE/6-311G**	DFTB	0.580	15.82E-3	-0.1195	0.991
PM3	DFTB	0.238	22.02E-3	-0.1485	0.993

Finally, we scale the overlap $|S_{AB}|$ for the semiempirical PM3 method to reproduce the DIPRO charge transfer integrals $|J_{AB}|$ on B3LYP/6-31G* level of theory (Fig. 3.20). We include all possible types of transitions that occur in the P3HT:DIPBI morphology. In the double logarithmic plot one can approximate the ascending $\log_{10} |J_{AB}|$ linearly by $\log_{10} |J_{AB}| = a \log_{10} |S_{AB}| + b$ with $a = 1.016$ and $b = 0.722$ for hole transfer and $a = 0.821$ and $b = 0.429$ for electron transfer. Both plots reveal a wide spreading of four to six orders of magnitude. This results in a small correlation coefficient for electron transfer ($R=0.83$) and a slightly enhanced value ($R=0.88$) for hole transfer. The values are both lower than those obtained for a direct scaling of $|J_{AB}|$. The quality of scaling $|S_{AB}|$ (PM3) to $|J_{AB}|$ (B3LYP/6-31G*) exceeds the quality of the geometric parametrisation of $|J_{AB}|$ (see Sec. 3.1.5). This finding is not surprising, as $|S_{AB}|$ includes information concerning the electronic structure, which cannot be provided by a simple set of structural parameters for a given pair of molecules.

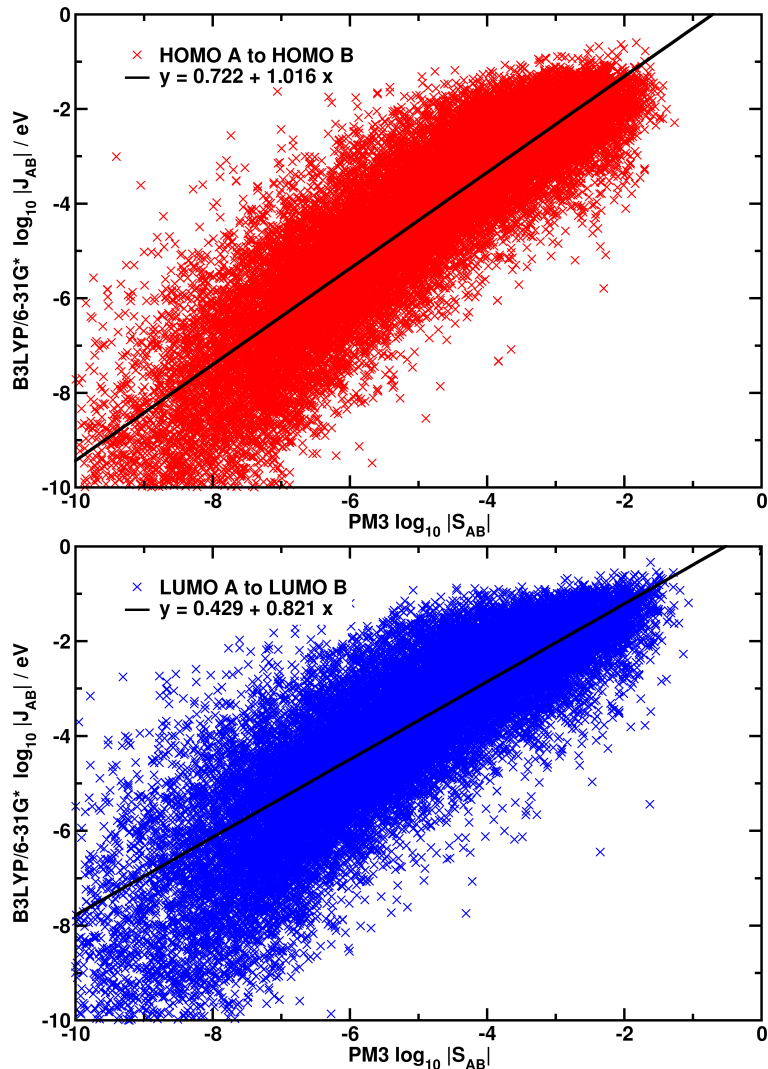


Figure 3.20: The DIPRO/B3LYP/6-31G* charge transfer integral $\log_{10} |J_{AB}|$ for hole (top) and electron transfer (bottom) as a function of the overlap $\log_{10} |S_{AB}|$ for PM3. The plot includes the data for pairs for the 12 nearest neighbours of every hopping site in the P3HT:DIPBI morphology.

3.1.7 Intramolecular Charge Transfer in P3HT Polymer Chains

The intramolecular charge transfer integral $|J_{\text{DA}}^{\text{int}}|$ and vertical energy gap $\Delta E_{\text{DA}}^{\text{int}}$ for P3MT with $n=2$ were calculated by CDFT/PBE as a function of the dihedral angles $\theta(\text{SCCS})$ between two linked thiophene units (Fig. 3.21). For this purpose, the dihedral angle $\theta(\text{SCCS})$ was rotated between -180° and 180° in steps of 2.5° . For each geometry, two CDFT calculations were carried out in which the excess charge is localized on the donor D and the acceptor A segment, respectively. Subsequently, the charge transfer integral $|J_{\text{DA}}^{\text{int}}|$ and the vertical energy gap $\Delta E_{\text{DA}}^{\text{int}}$ are evaluated using two diabatic wavefunctions. The CDFT-based charge transfer integrals $|J_{\text{DA}}^{\text{int}}|$ are interpolated using a spline fit function.

Figure 3.21 shows $|J_{\text{DA}}^{\text{h}}(\theta)|$ and $|J_{\text{DA}}^{\text{e}}(\theta)|$. We see that $|J_{\text{DA}}^{\text{h}}(\theta)|$ has a maximum value of $|J_{\text{max}}^{\text{h}}| = 2.97 \text{ eV}$ at $\theta \approx -180^\circ$, which corresponds to a planar configuration with the methyl groups on the same side of the chain. The value of $|J_{\text{DA}}^{\text{h}}(\theta)|$ then decreases with an increasing θ and reaches a minimum at -90° . It is worth noting that even at this orthogonal orientation of two thiophene rings, the charge transfer integral does not disappear completely, but remains at $|J_{\text{min}}^{\text{h}}| = 0.018 \text{ eV}$. A further increase in θ leads to a second, slightly lower maximum of $|J_{\text{DA}}^{\text{h}}| = 2.88 \text{ eV}$ at $\theta = 0^\circ$, in which the side methyl groups face away from each other (regioregular P3MT, Fig. 3.21 inset). Overall, the curve exhibits a mirror symmetry with respect to $\theta = 0^\circ$.

In general, the transfer integral for electrons reveals a similar trend as the data for hole transfer, but as the electron data yields more fluctuations, $|J_{\text{DA}}^{\text{e}}(\theta)|$ is interpolated by a cosine fit.

$$|J_{\text{DA}}^{\text{e}}(\theta)| = \begin{cases} 0.65 \text{ eV} |\cos(\frac{\pi}{180}\theta)| + 0.28 \text{ eV} & \text{for } -180^\circ < \theta < -90^\circ \vee 90^\circ < \theta < 180^\circ \\ 0.42 \text{ eV} |\cos(\frac{\pi}{180}\theta)| + 0.28 \text{ eV} & \text{for } -90^\circ \leq \theta \leq 90^\circ \end{cases} \quad (276)$$

The maximum $|J_{\text{max}}^{\text{e}}| = 0.96 \text{ eV}$ is about factor 3 lower and the minimum $|J_{\text{min}}^{\text{e}}| = 0.23 \text{ eV}$ remains about an order of magnitude higher, when compared to hole transfer data in configurations at $\theta \approx -180^\circ$ and $\theta \approx -90^\circ$, respectively.

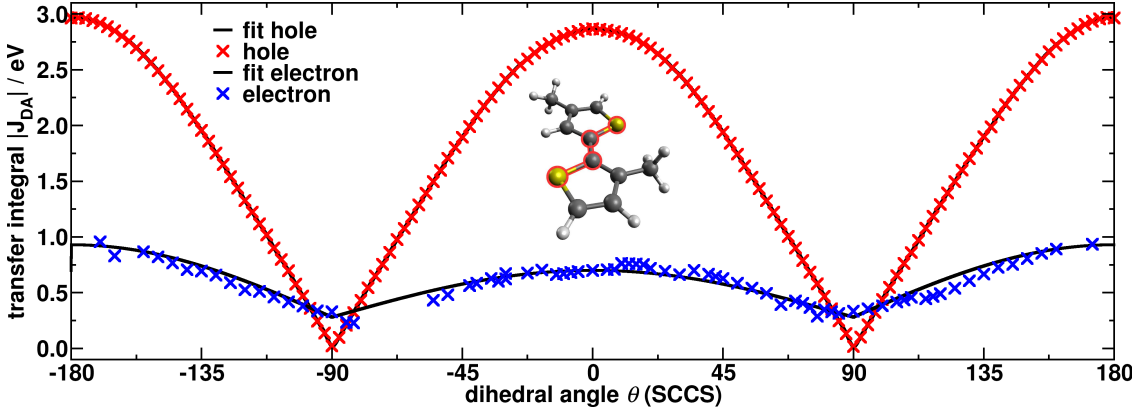


Figure 3.21: Intramolecular charge transfer integral $|J_{\text{DA}}^{\text{int}}|$ for hole transfer (red) and electron transfer (blue) in P3MT on the basis of CDFT/PBE. The excess charge is transferred between a donor P3MT segment D with $n_D = 1$ and an acceptor P3MT segment A with $n_A = 1$. The P3MT segments are rotated along the dihedral angle $\theta(\text{SCCS})$ (inset, red atoms). The CDFT data for hole transfer $|J_{\text{DA}}^{\text{h}}|$ is interpolated by a spline fit function and for electron transfer $|J_{\text{DA}}^{\text{e}}|$ a cosine fit is applied (Eq. 276). The CDFT data for hole transfer is provided by Tobias Lettmann [75].

The internal vertical energy gap $\Delta E_{\text{DA}}^{\text{int}}$ based on CDFT/PBE is displayed in Figure 3.22. The minimum vertical energy gap for hole transfer is $\Delta E_{\text{min}}^{\text{h}} = -0.11 \text{ eV}$ at $\theta \approx -180^\circ$. The value of $\Delta E_{\text{DA}}^{\text{int}}$ remains practically constant up to $\theta \approx -140^\circ$, then increases up to a maximum of 0.14 eV at $\theta \approx 0^\circ$, switching sign at $\theta \approx -85^\circ$. The slight asymmetry of the curve concerning $\theta = 0^\circ$ can be understood in terms of the underlying molecular asymmetry of the dithiophene. The CDFT data for hole transfer $\Delta E_{\text{DA}}^{\text{h}}$ is interpolated by a cubic spline fit function $f(\theta)$.

As the internal vertical energy gap for electron transfer $\Delta E_{\text{DA}}^{\text{e}}$ scatter more, the hole cubic spline fit $f(\theta)$ is scaled inversely to obtain $\Delta E_{\text{DA}}^{\text{e}}(\theta) = g(\theta) = -0.6f(\theta)$ for electron data interpolation. The function $g(\theta)$ exhibits a maximum at $\Delta E_{\text{max}}^{\text{e}} = 0.069 \text{ eV}$ at $\theta \approx -180^\circ$ and a minimum at $\Delta E_{\text{max}}^{\text{e}} = -0.086 \text{ eV}$ at $\theta \approx 0^\circ$.

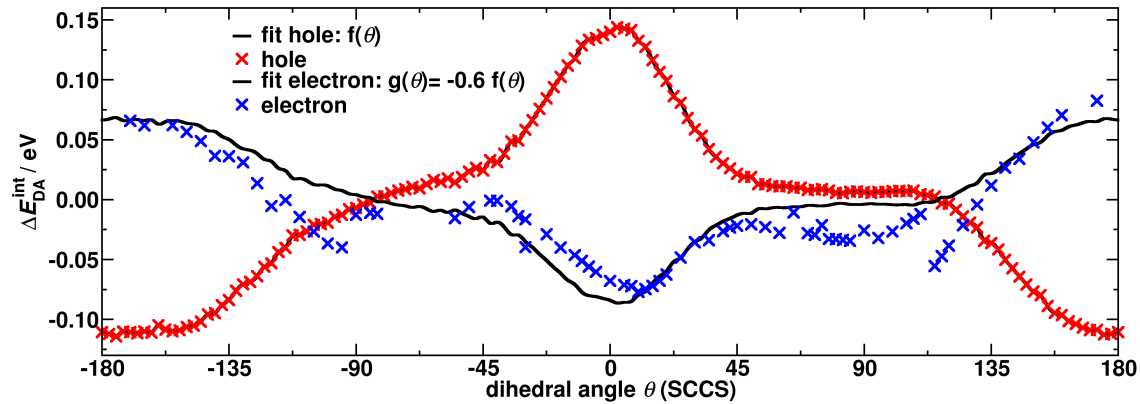


Figure 3.22: Vertical energy gap $\Delta E_{\text{DA}}^{\text{int}}$ for intramolecular hole transfer (red) and electron transfer (blue) in P3MT on the basis of CDFT/PBE. The excess charge is transferred between a donor D segment ($n_D = 1$) and an acceptor A segment ($n_A = 1$). The P3MT segments are rotated along the dihedral angle $\theta(\text{SCCS})$. The CDFT data for hole transfer $\Delta E_{\text{DA}}^{\text{h}}$ is interpolated by a spline fit function $f(\theta)$ and for electron transfer $g(\theta)$ the hole data is scaled as $\Delta E_{\text{DA}}^{\text{e}}(\theta) = g(\theta) = -0.6f(\theta)$.

In the kMC simulations of P3HT or P3HT:DIPBI morphologies, the above dihedral-dependent values of $|J_{\text{DA}}^{\text{int}}|$ and $\Delta E_{\text{DA}}^{\text{int}}$ are employed as follows. If a pair of two neighbouring P3HT segments in the morphology is separated by an angle θ_{SCCS} , which satisfies the cutoff criterion $\theta_{\text{SCCS}}^{\text{cut}}$ (Eq. 268), then the $|J_{\text{DA}}^{\text{int}}(\theta)|$ and $\Delta E_{\text{DA}}^{\text{int}}(\theta)$ values obtained from cubic spline fits to the respective data sets are used to evaluate intrachain hole and electron transfer rates k_{AB}^{int} . This procedure is applied irrespective of the length of the P3HT segments. A transition to a segment on the same chain that is not a direct lateral neighbour is made possible by a charge transfer integral $|J_{AB}|$ using DIPRO and is considered an intermolecular transfer.

In the following, we test the quality of this (1&1)-approximation on intramolecular transfer properties for predictions in segments with arbitrary length. Therefore, we extract four polymer chains from the atomistic P3HT:DIPBI morphology and evaluate the intramolecular charge transfer integrals (CDFT) on neighbouring P3MT segments, which are partitioned at cutoff angle $\theta_{\text{SCCS}}^{\text{cut}} = 75^\circ$. So, the segments can vary in their segment length $n_D \& n_A$ for every donor-acceptor pair. The results are compared to data (1&1)-approximation between two individual thiophene rings (Fig. 3.23). We see all $|J_{\text{DA}}^{\text{h}}|$ are at the same order of magnitude for $n_D \& n_A$ pairs as those for 1&1 around the orthogonal orientation for $\theta_{\text{SCCS}}^{\text{cut}}$. The $|J_{\text{DA}}^{\text{h}}|(n_D \& n_A)$ can exceed those for $|J_{\text{DA}}^{\text{int}}|(1&1)$ at the same θ .

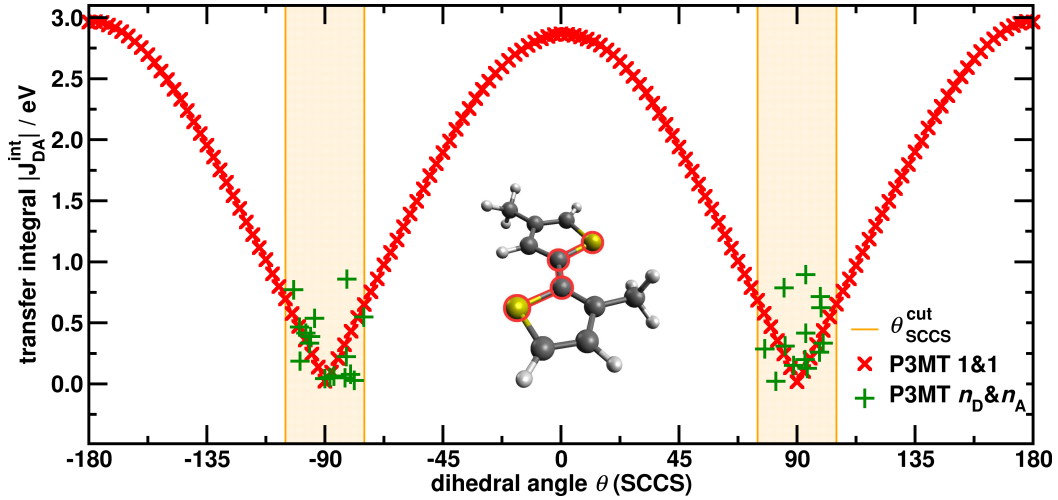


Figure 3.23: Intramolecular charge transfer integral (CDFT/PBE) for hole transfer between two P3MT units (1&1) as a function of the dihedral angle θ (SCCS) (inset). Several charge transfer integrals $|J_{DA}^h|(n_D \& n_A)$ for chain segments of different sizes n_D and n_A (green). The segments are extracted from the P3HT:DIPBI morphology using a partitioning at cutoff angle $\theta_{SCCS}^{cut} = 75^\circ$ (orange).

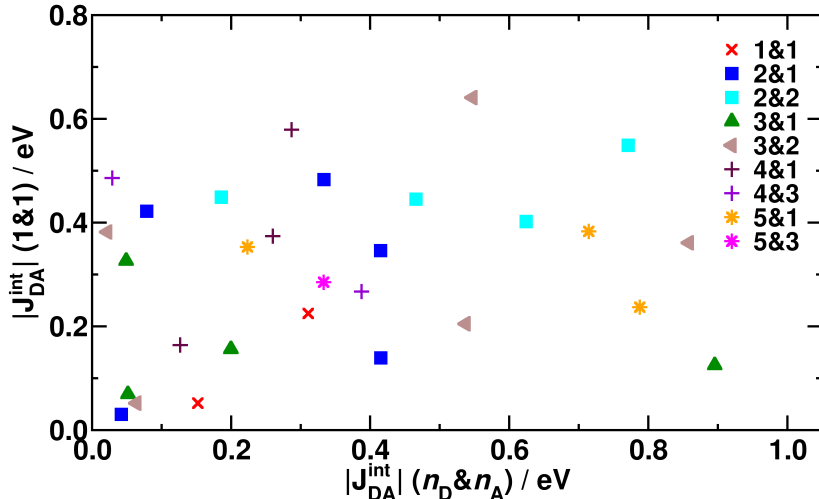


Figure 3.24: Comparison of several intramolecular charge transfer integrals $|J_{DA}^h|(n_D \& n_A)$ for chain segments of different sizes n_D and n_A to the (1&1)-approximation between two P3MT units at CDFT/PBE level of theory. The segments are extracted from the P3HT:DIPBI morphology using a partitioning at cutoff angle $\theta_{SCCS}^{cut} = 75^\circ$ (Eq. 268).

There is no direct correlation between the charge transfer integral for $n_D \& n_A$ and 1&1 (Fig. 3.24). Even for pairs that possess the same segment length ratio, we find a broad scattering in the data. This finding details, that θ_{SCCS} is the most critical degree of freedom with an impact on intrachain charge transfer in P3MT, but it is not the only one. However, the (1&1)-approximation yields reasonable predictions, as the order of magnitude of $|J_{AB}^{\text{int}}|$ is reproduced correctly. All in all, the determination of the charge transfer integral for intrachain transfer as a function of θ_{SCCS} in the 1&1 model is a suitable method to determine the correct order of magnitude of the electronic coupling.

The importance of variations in the torsion angle along the polymer backbone for intra-chain charge transport is undoubtedly [284]. The excess charge induces a chain planarization that goes along with a reduction of the amount of energetic disorder along the chain and in its environment [285, 286]. In the literature, the dihedral dependence of the intramolecular charge transfer integral has been approximated as [287]

$$J = J_0 \cos(\theta), \quad (277)$$

with $J_0 \approx 0.3$ eV estimated from the HOMO/HOMO-1 splitting using the fragment orbital approach. Alternatively, this dependence has been incorporated directly into the charge transfer rate [288, 289],

$$k_{AB} = \nu \exp \left[\frac{-(\Delta E_{AB} + \lambda_{AB})^2}{4\lambda_{AB}k_B T} - \frac{|J_0 \cos \theta|}{k_B T} \right] \quad (278)$$

with a prefactor $\nu = 10^{15}$ s⁻¹ and $J_0 = 1$ eV [290].

Our CDFT-based procedure goes beyond such ad-hoc approximations. It is applicable to all chain conformations found in the morphology and ensures the accessibility of all segments along the polymer chain to the excess charge. However, there is still space for further method development and a more refined parametrisation scheme for $|J_{AB}^{\text{int}}|$, e.g. as a function of thiophene chain length n , the intra-segment planarity P^b (see Eq. 279), segment bending angles or number of atoms N [75].

3.1.8 Conclusion: Charge Transfer Integral

We have investigated in detail the influence of different approaches from electronic structure theory and parametrisation schemes on the determination of the charge transfer integral.

We find the tendency of lower $|J_{AB}|$ in force-field generated structures compared to DFT-optimised structures based on acceptor dimers. If we apply DIPRO in conjugation with DFT, we see that the choice of the basis set is more important than the selected functional. The importance of the choice of the $|J_{AB}|$ calculation method is particularly evident in the $|J_{AB}|$ distribution of all pairs in the morphology. Since not only the magnitude of the $|J_{AB}|$ data changes, but also the shape of the distributions vary, the choice of method can influence the dynamics in kMC simulations. Thus, $|J_{AB}|^2$ as a pre-factor of k_{AB} not only exclusively provides a (linear) scaling of the order of magnitude in the simulated mobility.

We propose linear and non-linear scaling schemes for DIPRO-based charge transfer integrals $|J_{AB}|$ that link low cost, semiempirical approaches, DFTB and DFT to numerically demanding procedures as CDFT. We see that a parametrisation based on geometric quantities as different measures for the distance and for the relative orientation can only be employed as a rough estimate. Therefore, this method is only applied as a backup, if electronic structure calculations fail to converge.

The parametrisation of $|J_{AB}|$ as a function of the overlap $|S_{AB}|$ is more accurate, however it also requires a self-consistent calculation of the electron density and hence runs into the same problem of choosing a decent trade off between physical accuracy and computational costs. So, there is no clear advantage of calculating $|S_{AB}|$ and employing a scale instead of a directly calculating $|J_{AB}|$ by means of the DIPRO approach. One can see that simple, intuitive arguments are not sufficient to qualitatively predict the correlation between the local geometric structure of a polymer chain and the localisation of its frontier orbitals. Due to the proposed segmentation scheme of the polymer chain, where we employ a cutoff angle $\theta_{\text{SCCS}}^{\text{cut}}$ criterion in combination with the CDFT-based intra-chain charge transfer data, the charge can access the entire polymer chain in kMC simulations.

3.2 Internal Reorganization Energy and Internal Site-energy Difference

The reorganization energy and internal site-energy difference are evaluated based on the four-point schema depicted in Fig. 1.2. Geometry optimisations on single molecules in the gas phase are performed in the neutral, positive and negative charged states and four single-point calculations on the optimised structures are carried out in order to obtain λ^{in} and ΔE^{in} for hole and electron transfer. The standard method of choice for this purpose is DFT (Sec. 3.2.1).

If we start with P3MT polymer chains extracted from the atomistic morphology, the geometry optimisations result in a planarisation of the polymer backbone. Hence, the optimised structures of segments are not completely identical to those found in the crystalline phase. In this case, the segments do not fully relax to structures with alternating ring orientation, as the twists in the initial starting chain configuration indicate a relaxation to several local minimal on the ground state S_0 potential energy surface. As the presence of neighbouring molecules in the vicinity of a charge-transfer complex does not allow relaxation to planarity, a segmentation of the polymer chain is mandatory. Alternatively, the use of constraints is an option for more precise determination of λ^{in} and ΔE^{in} (Sec. 3.2.3).

An alternative approach to making the evaluation of λ^{in} and ΔE^{in} for individual hopping pairs inside the morphology feasible is using DFTB or universal force field (UFF) [276] based geometry optimisations and scale the results to DFT reference data (Sec. 3.2.2). Also, the application of constraints or the use of an ONIOM approach [261,262] to take the environmental effects on the geometry relaxation into account is discussed (Sec. 3.2.4).

3.2.1 Evaluation for P3HT:DIPBI within DFT

The internal reorganization energies λ_h^{in} , λ_e^{in} and internal site-energy difference ΔE_h^{in} , ΔE_e^{in} are calculated at DFT/B3LYP/6-311G** level of theory on the optimised structures of isolated molecules. The results are depicted in Figure 3.25 for the charge transfer of holes and electrons in the P3HT:DIPBI system. The data is plotted as a function of thiophene segment length n for different donor/acceptor pairs.

The internal reorganization energy is $\lambda_h^{\text{in}} = 0.130$ eV for hole transfer between two DIPBI molecules, whereas the reorganization energy for electron transfer is higher at $\lambda_e^{\text{in}} = 0.203$ eV. The influence of fluctuations in the side chains is of minor importance to the reorganization energy, as the reduction to methyl groups only leads to slightly lower values like $\lambda_h^{\text{in}} = 0.128$ eV for hole transfer and $\lambda_e^{\text{in}} = 0.202$ eV for electron transfer in DIPBI→DIPBI transitions.

As we can see from Figure 3.25, the reorganization energy is generally higher for hole transfer from DIPBI to P3MT than in the opposite direction, except for $n = 1$. A DIPBI→P3MT($n = 1$) transition yields $\lambda_h^{\text{in}} = 0.292$ eV. The DIPBI→P3MT curve exhibits a maximum of $\lambda_h^{\text{in}} = 0.514$ eV at $n = 3$ and decreases gradually with increasing n to $\lambda_h^{\text{in}} = 0.324$ eV for $n = 20$ (Fig. 3.25,i, red curve). In the inverse reaction (P3MT→DIPBI), the reorganization energy decreases from $\lambda_h^{\text{in}} = 0.308$ eV at $n = 1$ with increasing n to $\lambda_h^{\text{in}} = 0.163$ eV at $n = 20$ (Fig. 3.25,i, orange curve).

The reorganization energies for electron transfer are slightly higher than the corresponding values for hole transfer. For electron transfer (Fig. 3.25,ii, cyan) from DIPBI to P3MT($n = 1$), we obtain $\lambda_e^{\text{in}} = 0.454$ eV. The maximum is $\lambda_e^{\text{in}} = 0.461$ eV for DIPBI to P3MT($n = 3$) transitions, and we apply the value $\lambda_e^{\text{in}} = 0.309$ eV for long chains with $n > 20$.

The inverse reaction $\text{P3MT}(n=1) \rightarrow \text{DIPBI}$ gives $\lambda_e^{\text{in}} = 0.756$ eV, a $\text{P3MT}(n=3) \rightarrow \text{DIPBI}$ transition results in $\lambda_e^{\text{in}} = 0.290$ eV, and one approaches a limit of $\lambda_e^{\text{in}} = 0.197$ eV (Fig. 3.25,ii, blue) with increasing n . As the reorganization energy is practically converged asymptotically for $n=20$, the same value is applied for $n \in [21, 32]$.

The internal site-energy difference ΔE_h^{in} for hole transfer from DIPBI to P3MT decays with a rising thiophene segment length n and reaches the asymptotic value of $\Delta E_h^{\text{in}} = -2.036$ eV for $n=20$ (Fig. 3.25,iii, red line). The positive value for $\text{DIPBI} \rightarrow \text{P3MT}(n=1)$ of $\Delta E_h^{\text{in}} = 1.180$ eV is an exception, as all other values (for $n > 1$) are negative, favouring hole transfer from the DIPBI to the P3HT segments. For instance, the DIPBI to a $\text{P3MT}(n=3)$ transition yields $\Delta E_h^{\text{in}} = -0.740$ eV. The values for ΔE_h^{in} for hole transfer from P3MT to DIPBI possess positive sign due to $\Delta E_h^{\text{in}}(\text{AB}) = -\Delta E_h^{\text{in}}(\text{BA})$.

The site-energy difference ΔE_e^{in} for electron transfer from P3MT to DIPBI rises with an increasing polymer segment length n (Fig. 3.25,iv, blue line). It yields a values of $\Delta E_e^{\text{in}} = -4.872$ eV for $\text{P3MT}(n=1) \rightarrow \text{DIPBI}$, and rises to $\Delta E_e^{\text{in}} = -1.610$ eV for $n=20$ in the asymptotic limit. The $\text{DIPBI} \rightarrow \text{DIPBI}$ transitions always give $\Delta E_{h/e}^{\text{in}} = 0.0$ eV.

These trends are in accordance with the expected preferential transfers direction $\text{DIPBI} \rightarrow \text{P3HT}$ for holes and $\text{P3HT} \rightarrow \text{DIPBI}$ for electrons at the donor/acceptor interface. The values for λ_h^{in} , λ_e^{in} , ΔE_h^{in} , ΔE_e^{in} with all possible donor/acceptor pair combinations AB and BA are stored in 33×33 matrices and accessed to evaluated Marcus charge transfer rates in kMC simulations. These datasets are applied to all pairs, regardless of relative orientation, conformation or embedding within the morphology.

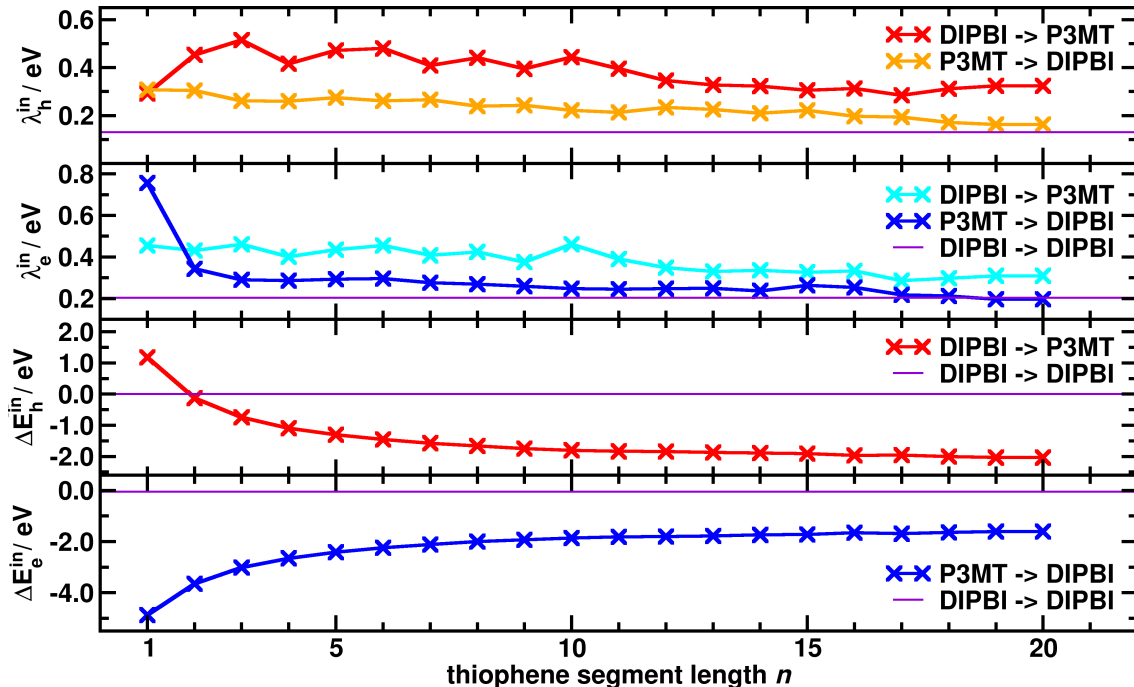


Figure 3.25: Internal reorganization energy λ_h^{in} , λ_e^{in} , and internal site-energy difference ΔE_h^{in} , ΔE_e^{in} for hole and electron charge transfer as a function of the number of thiophene units n in a P3MT chain. The data is based on DFT/B3LYP/6-311G**. Transitions for hole transfer between $\text{DIPBI} \rightarrow \text{P3MT}$ (red), $\text{P3MT} \rightarrow \text{DIPBI}$ (orange) and $\text{DIPBI} \rightarrow \text{DIPBI}$ (violet) and transitions for electron transfer $\text{DIPBI} \rightarrow \text{P3MT}$ (cyan), $\text{P3MT} \rightarrow \text{DIPBI}$ (blue) and $\text{DIPBI} \rightarrow \text{DIPBI}$ (violet) are taken into account. The sign of the internal site-energy difference is reversed $\Delta E_{h/e}^{\text{in}}(\text{AB}) = -\Delta E_{h/e}^{\text{in}}(\text{BA})$, if the charge transfer direction is reversed.

3.2.2 Evaluation for P3HT:DIPBI within DFTB

The internal reorganization energy λ^{in} and the internal site-energy difference ΔE^{in} based on DFTB/Mio-1-1 are depicted in Fig. 3.26 for hetero-molecular DIPBI→P3MT and P3MT→DIPBI transitions. The DFTB data shows basically the same dependence of λ^{in} on the thiophene segment length n , as the DFT-based data and can be extended to evaluate λ^{in} and ΔE^{in} up to $n=32$. The DFTB reorganization energies λ_h^{in} are about a factor 5 and λ_e^{in} about a factor 4 lower, than the corresponding data on B3LYP/6-311G** level of theory. The $\lambda_h^{\text{in}} = 0.055$ eV is about half of the $\lambda_h^{\text{in}} = 0.115$ eV value for DIPBI→DIPBI transitions. DIPBI→P3MT and P3MT→DIPBI transitions show similar trends for λ_h^{in} and λ_e^{in} . In the long-chain limit, the reorganization energies decay to $\lambda_h^{\text{in}} = 0.04$ eV and $\lambda_e^{\text{in}} = 0.07$ eV.

In the same way, the DFTB-based ΔE_h^{in} and ΔE_e^{in} (Fig. 3.26) exhibit similar trends as the corresponding DFT data (Fig. 3.25). Similarly, the internal site-energy difference tends towards negative values of $\Delta E_h^{\text{in}} = -2.33$ eV and $\Delta E_e^{\text{in}} = -0.61$ eV in the long-chain limit.

The calculations of λ^{in} and ΔE^{in} with the UFF model result in similar trends as with DFTB, but exhibit stronger fluctuations as a function of n with up to 0.1 eV. Therefore, the UFF data is not considered in more detail.

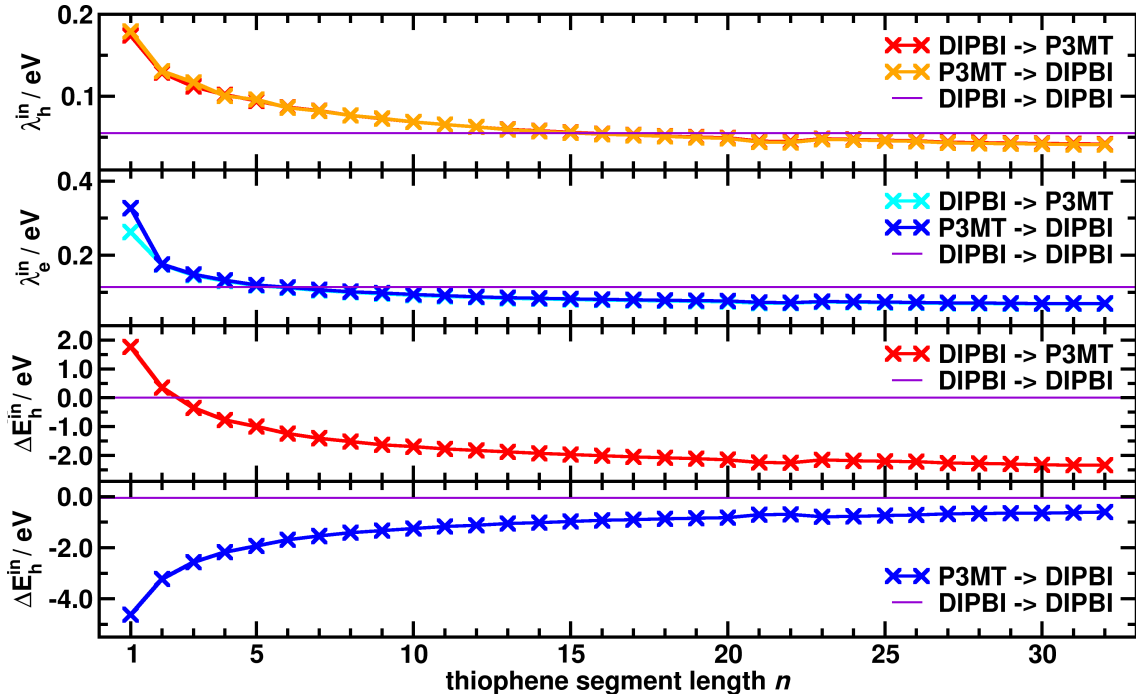


Figure 3.26: Internal reorganization energy λ_h^{in} , λ_e^{in} , and internal site-energy difference ΔE_h^{in} , ΔE_e^{in} for hole and electron charge transfer as a function of the number of thiophene units n in a P3MT chain. The data is based on DFTB/Mio-1-1. Transitions for hole transfer between DIPBI→P3MT (red), P3MT→DIPBI (orange) and DIPBI→DIPBI (violet) and transitions for electron transfer DIPBI→P3MT (cyan), P3MT→DIPBI (blue) and DIPBI→DIPBI (violet) are taken into account. The sign of the internal site-energy difference is reversed $\Delta E_{h/e}^{\text{in}}(AB) = -\Delta E_{h/e}^{\text{in}}(BA)$, if the charge transfer direction is reversed.

3.2.3 Evaluation for P3HT with Constraints

In the following, we will discuss the influence of position constraints on the optimised geometries and the resulting impact on reorganization energies for a pair of P3MT chains with a thiophene segment length $n=11$ and $n=19$. We compare the initial MM geometry to the free DFT-optimised structure, and test two different constraints α_{cons} and β_{cons} . On the one hand, we employ a first curvature constraint α_{cons} and fix a carbon atom C_α at every third thiophene ring along the polymer backbone for a P3MT with $n=11$ at index $\alpha \in \{6, 36, 66, 86, 106\}$ and a P3MT with $n=19$ at index $\alpha = \{6, 46, 86, 126, 166, 186\}$, respectively. On the other hand, we employ a position constraint β_{cons} on the carbon atoms of every lateral methyl group along the polymer chain, which should mimic an allowed relaxation of the nuclear degrees of freedom along the polymer backbone. Moreover, the constraint hinders vast segment reorientations on the time scales of charge transfer processes due to the rigid embedding of the side-chains in the device morphology. The carbon atoms with index $\beta_{\text{cons}} \in \{8 + 10(i-1)\}$ are fixed for every i -th thiophene unit in P3MT $n=11$ and $n=19$, respectively. The constrained geometry optimisations are performed for both charged and neutral systems.

We employ the planarity descriptor P^\flat , which takes all dihedral angles θ_i^{SCCS} into account between two neighbouring thiophene units along a polymer chain [291].

$$P^\flat = \sum_i^{n-1} \frac{||\theta_i^{\text{SCCS}}| - 90|}{90} \quad \text{with } \theta_i^{\text{SCCS}} \in [-180, 180] \quad (279)$$

The descriptor P^\flat is a measure of planarity. The contribution of a junction between two thiophene rings i with θ_i^{SCCS} to the total sum is zero, where both rings are totally out-of-plane with each other and one where they are absolutely planar. The minimum value $P^\flat = 0$ indicates a completely broken conjugated π -system independent of the segment length n . The maximum value is $P^\flat = n - 1$, meaning that longer chains can exhibit a higher measure of planarity.

The initial curved and twisted geometry for a selected P3MT with $n=11$ is extracted from the atomistic morphology (Fig. 3.27,i), and it relaxes to a nearly planer chain in QM ground state S_0 geometry optimisation (Fig. 3.27,ii). The QM structure maintains a small end-to-end bending and a non-symmetric alternating alignment of the thiophene units. The higher degree of planarisation is also reflected in the higher descriptor $P^\flat = 6.25$ (QM) compared to $P^\flat = 2.36$ (MM). In contrast, the constraint α_{cons} helps to maintain the overall polymer chain curvature in the morphology and causes a smoother, steady alignment of neighbouring thiophene units. This enhances the planarity $P^\flat = 5.56$ compared to MM, which is a feature that facilitates the excess charge delocalisation (Fig. 3.27,iii). Some thiophene units can flip the orientation using α_{cons} . The optimisation with β_{cons} also leads to a flattening in the ring-ring connections compared to MM geometry and increases the planarity ($P^\flat = 3.38$). In return, this advantage is conserved to maintain general predominant alignment direction of the thiophene rings (Fig. 3.27,iv), which is not the case for α_{cons} . Similar trends are also found for P3HT $n=19$.

Comparison of the free internal reorganization energy $\lambda_{\text{free}}^{\text{in}}$ and the constrained $\lambda_{\alpha_{\text{cons}}}^{\text{in}}$ for a $n=11$ to $n=19$ transition results in a decrease of the reorganization energy (Tab. 3.8). As the constraint on $\lambda_{\beta_{\text{cons}}}^{\text{in}}$ reduces the flexibility, the resulting reorganization energies are lower in comparison to $\lambda_{\alpha_{\text{cons}}}^{\text{in}}$ and $\lambda_{\text{free}}^{\text{in}}$, respectively. On average, α_{cons} and β_{cons} result in a decrease of the reorganization energy about 0.12 eV and 0.22 eV with respect to $\lambda_{\text{in}}^{\text{free}}$.

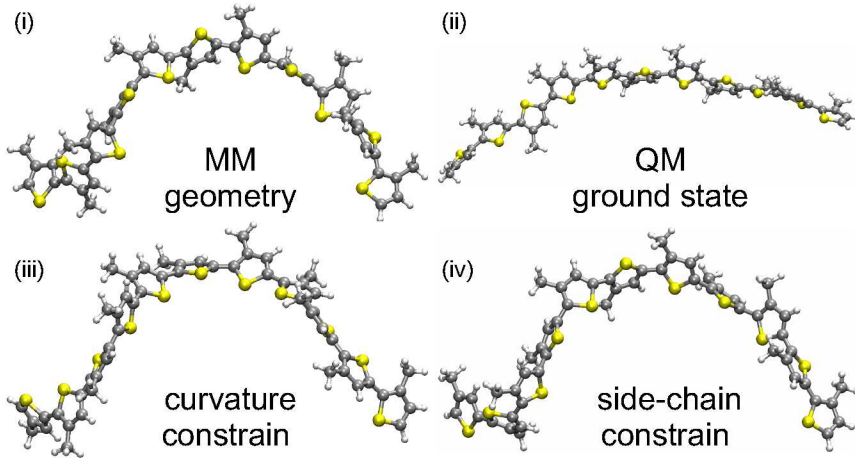


Figure 3.27: Comparison of geometric structures of a P3MT $n = 11$ chain as (i) the initial MM geometry extracted from the atomistic morphology, (ii) the optimised QM ground state S_0 geometry. (iii) the QM optimised geometry with a constraint α_{cons} to maintain the overall chain curvature in the morphology and (iv) QM optimised geometry with a side-chain constrain β_{cons} . The QM calculations are performed on B3LYP/6-311G** level of theory.

The DFTB $\lambda_{\text{free}}^{\text{in}}$ result in similar reorganization energies in $A \rightarrow B$ and $B \rightarrow A$ direction. On average the DFTB $\lambda_{\text{free}}^{\text{in}}$ are about 0.34 eV lower than the corresponding DFT data. The application of constraints results for DFTB in an increase in $\lambda_{\alpha_{\text{cons}}}^{\text{in}}$ about 0.02 eV with respect to $\lambda_{\text{free}}^{\text{in}}$, whereas the internal site-energy differences $\Delta E^{\alpha_{\text{cons}}}$ are slightly reduced. The DFTB calculations with β_{cons} do not converge to a local minimum in the charged state.

Table 3.8: Free internal reorganization energy $\lambda_{\text{free}}^{\text{in}}$ for hole and electron transfer, constrained reorganization energies $\lambda_{\alpha_{\text{cons}}}^{\text{in}}$ and $\lambda_{\beta_{\text{cons}}}^{\text{in}}$, and internal site-energy difference for a pair of neighbouring P3MT polymer chains A and B with a thiophene segment length $n = 11$ and $n = 19$, respectively. The data is presented on DFT/B3LYP/6-311G** and DFTB/MIO-1-1 level of theory for comparison.

	DFT			DFTB	
	$\lambda_{\text{free}}^{\text{in}}$ [eV]	$\lambda_{\alpha_{\text{cons}}}^{\text{in}}$ [eV]	$\lambda_{\beta_{\text{cons}}}^{\text{in}}$ [eV]	$\lambda_{\text{free}}^{\text{in}}$ [eV]	$\lambda_{\alpha_{\text{cons}}}^{\text{in}}$ [eV]
λ_{AB}^h	0.409	0.382	0.094	0.061	0.080
λ_{BA}^h	0.430	0.298	0.225	0.060	0.079
ΔE_{AB}^h	0.199	0.266	0.231	0.341	0.294
λ_{AB}^e	0.352	0.275	0.208	0.052	0.071
λ_{BA}^e	0.384	0.144	0.151	0.052	0.071
ΔE_{AB}^e	0.205	0.455	0.382	0.327	0.302

In conclusion, the application of the constraints α_{cons} and β_{cons} results in a reduction of the reorganization energies. They guarantee the conservation of the end-to-end bending in the polymer chain upon charge transfer. Hence, they provide a more accurate description of the underlying physical process than calculations on unconstrained, isolated molecules. The DFTB calculations are not a good approximation for the higher level DFT results and are therefore not used as a substitute for DFT, although DFTB is computationally cheaper.

3.2.4 Evaluation in a Molecular Environment within ONIOM

The morphological environment hinders the relaxation of a molecule during charge transfer and influences λ^{in} when the charge-transfer complex is embedded in a cavity of neighbouring molecules. Therefore, it is essential to estimate the energetic magnitude of this impact compared to calculations on vacuum level.

Another method to evaluate the internal reorganization energy is the use of a QM:MM approach, where the hopping sites A and B in the charge-transfer complex containing the excess charge are regarded as the QM regions and the environment in a shell of molecules around is treated as the MM region. While optimising geometry A at the electronic state of interest $c = \{n, h, e\}$ as a high-level QM region, the geometry of B and the atoms in the environment are frozen in the low-level MM regions and vice versa.

The third layer of theory can be introduced using a polarisable continuum model (PCM), which requires the dielectric constant ϵ for the environment. The four-point schema is applied in conjugation with QM:MM:PCM calculations to determine $\lambda_{\text{ONIOM}}^{\text{in}}$ and $\Delta E_{\text{ONIOM}}^{\text{in}}$ for hole or electron transfer between two hopping sites (see Fig. 1.2). If the excess charge is located on a segment inside the P3HT polymer chain backbone, then additional virtual H atoms are applied to saturate the segment margins in the QM calculations.

Reorganization Energies in the ONIOM model The free reorganization energies $\lambda_{\text{free}}^{\text{in}}$ and $\lambda_{\text{ONIOM}}^{\text{in}}$ are calculated on the basis of ONIOM(PBE0/6-31G*:UFF:PCM) using PBE0/CHelpG partial charges with 17 neighbouring molecules inside a cutoff radius with a $d_{\text{COM}} \leq 15 \text{ \AA}$ (Tab. 3.9). In the ONIOM ground state geometry optimisations, one can observe a planarisation of the selected QM section along the polymer backbone. In general, the restriction of the environment in the relaxation process causes a reduction in the reorganization energy $\lambda_{\text{ONIOM}}^{\text{in}}$ about $\approx 0.1 \text{ eV}$, when compared to gas phase $\lambda_{\text{free}}^{\text{in}}$.

As atomic partial charges are now included in the morphology environment of the charge-transfer complex, the internal site-energy difference ΔE_{ONIOM} is also altered. The magnitude of ΔE_{ONIOM} is also comparable to the magnitude in the outer-sphere contributions. Hence, it can influence the predominant direction of charge transfer reactions. One needs to avoid double counting of outer-sphere effects when using ΔE_{ONIOM} in conjunction with ΔE^{out} in Marcus rates for kMC simulations.

Table 3.9: Free internal reorganization energy $\lambda_{\text{free}}^{\text{in}}$ for hole and electron transfer and three layer QM:MM:PCM reorganization energy $\lambda_{\text{ONIOM}}^{\text{in}}$ and internal site-energy difference ΔE_{ONIOM} within a MM environment, using the ONIOM(PBE0/6-31G*:UFF:PCM) approach for a pair of P3MT segments A and B with a segment length $n_A = 1$ and $n_B = 1$, respectively. The MM region includes 17 molecules located within a cutoff radius $d_{\text{COM}} \leq 15 \text{ \AA}$.

	Free DFT [eV]	ONIOM(QM:MM:PCM) [eV]
λ_{AB}^h	0.4708	0.410
λ_{BA}^h	0.4710	0.409
ΔE_{AB}^h	-3.91E-5	-0.179
λ_{AB}^e	1.0352	0.821
λ_{BA}^e	1.0370	0.863
ΔE_{AB}^e	1.69E-5	-0.110

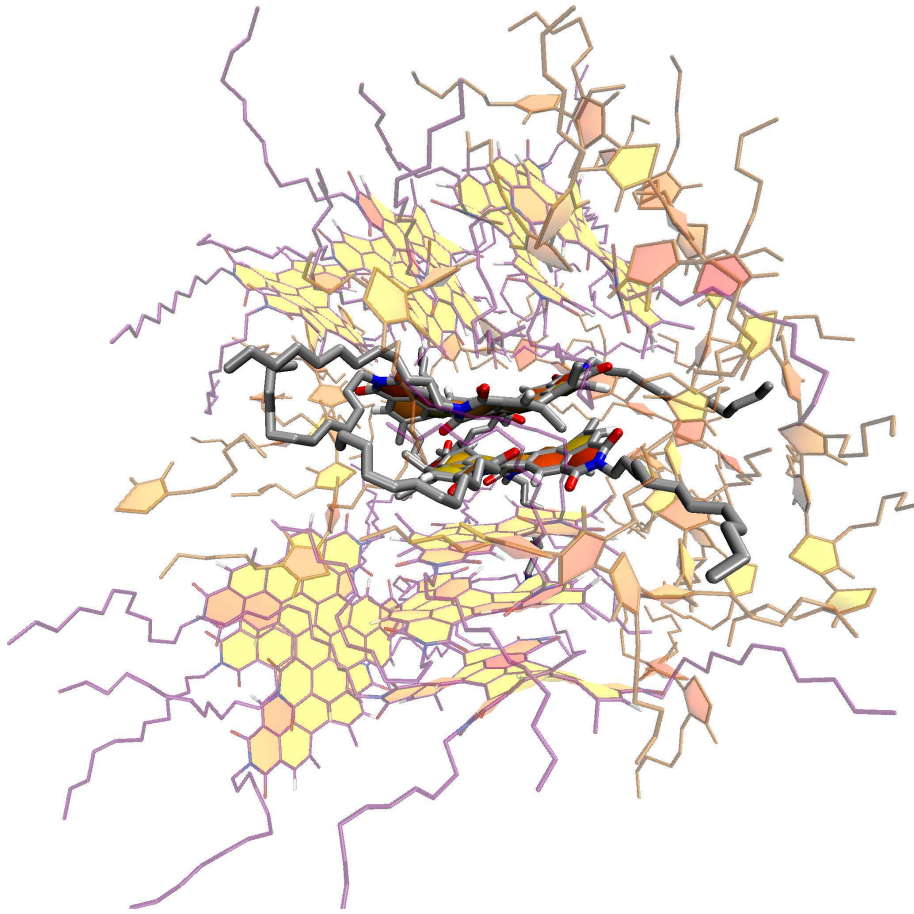


Figure 3.28: Selected DIPBI/DIPBI charge transfer dimer (grey) inside the cavity of molecules within a COM cutoff radius about $d_{\text{COM}} \leq 20 \text{ \AA}$ inside the P3HT:DIPBI morphology. DIPBI (violet) and P3HT segments (orange) are coloured in the paper chain representation to display the molecular planes and the π -stacking orientation. The DIPBI/DIPBI are treated as QM region and the other molecules are regarded as MM region in the ONIOM calculations for $\lambda_{\text{ONIOM}}^{\text{in}}$ and ΔE_{ONIOM} .

Similarly, we perform evaluations for the reorganization energy using the three-level ONIOM(B3LYP/6-31G*:UFF:PCM) approach for a pair of DIPBI molecules, which are embedded in a π -stack inside the P3HT:DIPBI morphology (Fig. 3.28). A cutoff radius for the molecules in the MM region around the charge-transfer complex about $d_{\text{COM}} \leq 20 \text{ \AA}$ is selected, which results in 13 DIPBI molecules and several P3HT chain segments including 58 thiophene units in total.

We compare the reorganization energies of an isolated pair of DIPBI molecules to those of an embedded pair. We notice that the surrounding environment induces an asymmetry in the reorganization energies and hence a slightly preferential direction of charge transfer. Whereas, both charge transfer directions are equivalent for isolated pairs (Tab. 3.10). In total, the $\lambda_{\text{ONIOM}}^{\text{in}}$ deviate from the unconstrained $\lambda_{\text{free}}^{\text{in}}$ about 0.01 eV to 0.02 eV. $\lambda_{\text{BA}}^{\text{h}}$ yields a favourable, lower value about 0.028 eV in B→A direction than in the reversed case. Moreover, the reorganization energy for electron transfer $\lambda_{\text{AB}}^{\text{e}}$ is 0.037 eV lower than for the opposite direction.

Table 3.10: Free internal reorganization energy $\lambda_{\text{free}}^{\text{in}}$ (B3LYP/6-31G*) for hole and electron transfer and three layer QM:MM:PCM reorganization energy $\lambda_{\text{ONIOM}}^{\text{in}}$ and internal site-energy difference ΔE_{ONIOM} with a QM embedding in a MM environment, using the ONIOM(B3LYP/6-31G*:UFF:PCM) approach for a pair of DIPBI molecules ($\text{A} \leftrightarrow \text{B}$). The MM region includes 17 molecules located within a cutoff radius $d_{\text{COM}} \leq 20 \text{ \AA}$.

	DFT [eV]	QM:MM:PCM [eV]
$\lambda_{\text{AB}}^{\text{h}}$	0.196	0.209
$\lambda_{\text{BA}}^{\text{h}}$	0.196	0.181
$\Delta E_{\text{AB}}^{\text{h}}$	0.003	0.003
$\lambda_{\text{AB}}^{\text{e}}$	0.124	0.105
$\lambda_{\text{BA}}^{\text{e}}$	0.124	0.142
$\Delta E_{\text{AB}}^{\text{e}}$	0.008	-0.008

All in all, the ONIOM calculations detail that the steric hindrance of the surrounding cavity influences the relaxation process of the molecules inside the morphology upon charge transfer and hence can evoke alterations in λ^{in} and even induce an asymmetry in the charge transfer direction.

3.2.5 Conclusion: Internal Reorganization Energy and Internal Site-energy Difference

We determined the internal reorganization energy in P3HT:DIPBI using DFT or DFTB on vacuum level and modelled environmental hindrance to molecular relaxation using geometric constraints or a fixed molecular cavity within the ONIOM approach. We see that, the steric hindrance of the polymer side chain inside the amorphous or crystalline morphology prevents the polymer from undergoing large conformational changes upon charging and discharging. Therefore, the reorganization energy is reduced as a result of conformational constraints. All in all, the explicit evaluation of individual DFT-based λ^{in} and ΔE^{in} is not feasible for all charge transfer pair inside the entire morphology. The attempt to replace computational expensive DFT calculations by cheaper DFTB or UFF results is discarded due to the limited accuracy compared to DFT. Even though the values of λ^{in} influence the Marcus rates significantly, an explicit treatment is omitted in the following kMC simulations, as it is common practice in literature [57, 190, 292].

3.3 Hopping Site Distance

The distance dependence of charge transfer rates k_{AB} is known from early theoretical approaches [293, 294] and experimental investigations [295–297]. The question arises how to determine \mathbf{d}_{AB} for hopping pairs inside an amorphous morphology. Due to limited computational resources, we cannot employ an electron density-based method to evaluate \mathbf{d}_{AB} for all possible hopping pairs.

Instead, we use geometric distance definitions based on the positions of the nuclei to approximate the charge transfer distance by d_{COM} (Eq. 275), d_{MA} (Eq. 273) and d_{MMA} (Eq. 274) as a first guess. Moreover, we introduce a thiophene ring-based centre of mass (RCOM) distance \mathbf{d}_{RCOM} (Eq. 280). Next, we take a closer look at an outtake from the P3HT:DIPBI morphology (Fig. 3.29), which focuses on a central DIPBI molecule and the nearest neighbours.

The graphic includes the centre of masses (yellow points), which are located usually at the central plane of DIPBI molecules. In contrast, if P3HT polymer chains possess kinks or bends, then the COM of entire segments can be located outside of the polymer backbone. Hence, in some cases the distance d_{COM} only provides limited information for the charge transfer process. As an attempt to overcome this deficiency, we define a local centre of mass for every thiophene ring \mathbf{R}^{ring} along the polymer backbone (Fig. 3.29, orange points), omitting the attached side chains in the evaluation of \mathbf{R}^{ring} . For charge transfer between two hopping sites A and B with a thiophene segment length n_A and n_B , we define the ring centre of mass distance,

$$d_{\text{RCOM}} = |\mathbf{d}_{\text{RCOM}}| = \min|\mathbf{R}_i^{\text{ring}} - \mathbf{R}_j^{\text{ring}}| \quad \text{with } i \in [1, n_A] \text{ and } j \in [1, n_B], \quad (280)$$

as the minimal distance between pairs of these local ring centres. If A or B is not a thiophene segment, then the centre of mass \mathbf{R}^{COM} replaces \mathbf{R}^{ring} . All ring centres $\{\mathbf{R}^{\text{ring}}\}$ that belong to neighbouring segments of the central DIPBI, which meet the distance criterion for d_{RCOM} , are highlighted as yellow points (Fig. 3.29).

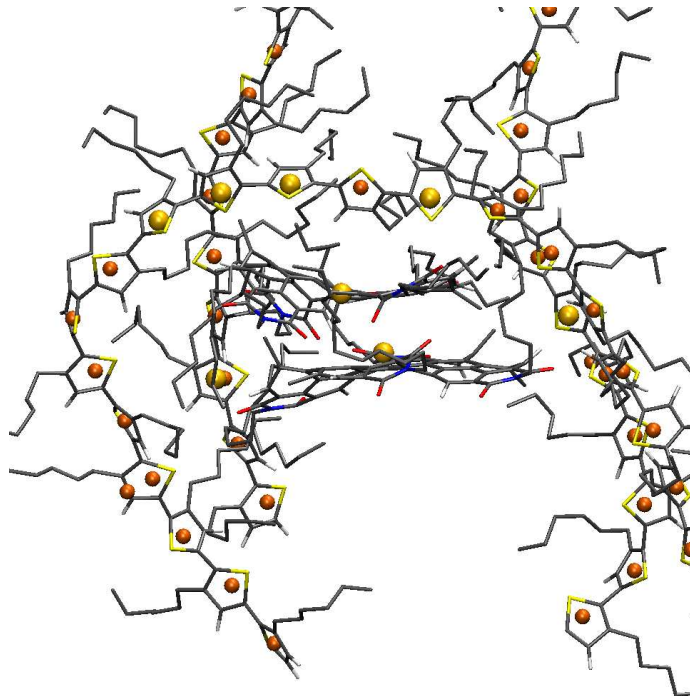


Figure 3.29: Outtake of the P3HT:DIPBI morphology in the vicinity of a central DIPBI molecule with the centre of masses (orange, yellow points) for neighbours. The centres of thiophene ring \mathbf{R}^{ring} are marked in orange. Centres from segments \mathbf{R}^{ring} that meet the distance criterion for ring centres $|\mathbf{d}_{\text{RCOM}}|$ (Eq. 280) are highlighted in yellow. These nearest neighbours of the central DIPBI molecule are taken into account in the neighbour list to evaluate charge transfer rates.

We evaluate the distances d_{COM} , d_{MA} , d_{MMA} and d_{RCOM} for all charge transfer pairs within a COM cutoff distance $r_{\text{cut}}^{\text{NN}} = 15 \text{ \AA}$ to neighbouring hopping sites (see Sec. A.1.5), and compare both their distance distributions and the associated rates (Fig. 3.30). The distribution for d_{COM} is broad and centred at an average distance of $\bar{d}_{\text{COM}} = (11.3 \pm 3.5) \text{ \AA}$ (Fig. 3.30,i).

The minimal distances are shifted to lower values, and yield the average $\bar{d}_{\text{MA}} = (4.8 \pm 2.1)$ Å with an accumulation point at $d_{\text{MA}} = 2.8$ Å. The mean minimal appearing distance is centred at $\bar{d}_{\text{MMA}} = (8.4 \pm 2.7)$ Å between the distributions for d_{MA} and d_{COM} . The distribution for RCOM exhibits a similar shape as MMA, except for the local maximum at $d_{\text{RCOM}} = 7.2$ Å. The distribution is shifted to a higher value $\bar{d}_{\text{RCOM}} = (9.1 \pm 2.9)$ Å.

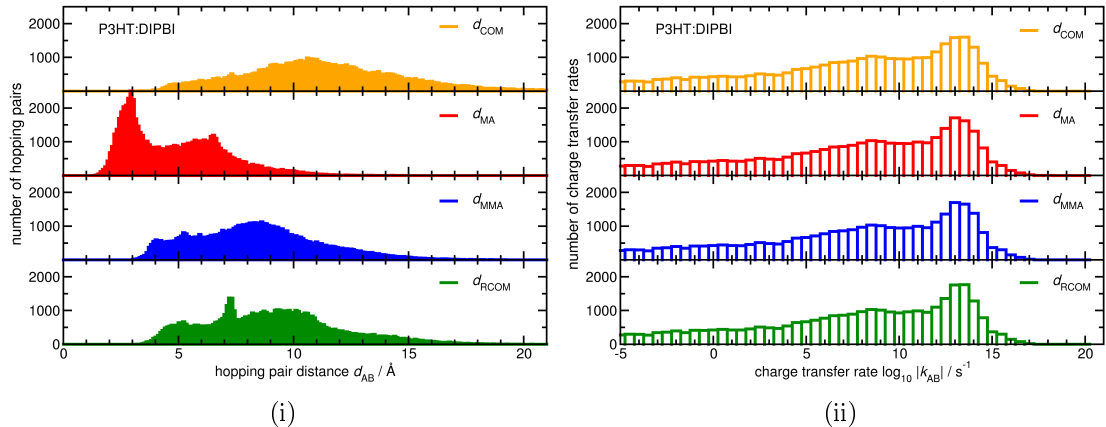


Figure 3.30: (i) Distributions of hopping pair distances $d_{AB} = |\mathbf{d}_{AB}|$ for hopping pairs inside a P3HT:DIPBI morphology. We compare the minimal appearing distance d_{MA} , the mean minimal appearing distance d_{MMA} , the centre of mass distances d_{COM} and the thiophene ring COM distance d_{RCOM} . (ii) Marcus rate distributions $\log_{10} k_{AB}$ for different distances.

As the distributions of the hopping site distances differ significantly, the choice of d_x also influences the ΔE^{ext} term (Eq. 201) and thus alters the charge transfer rates (Fig. 3.30,ii). At first glance, the distributions of the Marcus rates $\log_{10} k_{AB}$ for the different distances do not vary a lot. We employ the log-average

$$h_x = \exp \left(\frac{1}{N} \sum_{i=1}^N \log k_{AB}(d_{\text{COM}}) - \log k_{AB}(d_x) \right) \quad \text{with } x \in [\text{MA}, \text{MMA}, \text{RCOM}] \quad (281)$$

in order to quantify the difference in the rate distributions between d_{COM} and the distance measures MA, MMA and RCOM. We obtain a value of $h_{\text{MA}} = 1.015$, which details that the rates are on average 2% higher using MA compared to COM. In contrast, both MMA and RCOM exhibit lower values to about the same extend, as they yield $h_{\text{MMA}} = 0.985$ and $h_{\text{RCOM}} = 0.986$.

The choice to determine the distances d results in alternations of the rates and hence influences the simulated charge carrier dynamics. This factor is especially relevant, if the magnitude of ΔE^{ext} and $\Delta E_{AB}^{\text{in}}$ are at the order as λ , which can lead to a (counterintuitive) increase in the rates with increasing hopping distance. However, ΔE^{ext} yields the smallest contribution to the rate at a moderate external field, when compared to other quantities (see Sec. 4.2.2).

At this stage, it is not clear, which distance criterion yields the best description for charge transfer. Therefore, we use the COM definition, as it is common practice in literature [56,57,282], or the refined RCOM approach. In total, we employ a geometric criterion based on nuclear coordinates in the multiscale model to approximate the charge transfer hopping distance.

3.4 Comparison of Charge Transfer Rate Expressions

In the next section, we compare Marcus transfer rates to Weiss-Dorsey rates and Levich-Jortner rates (Sec. 1.4.2). Both latter cases remedy some deficiencies in Marcus approach. The Weiss-Dorsey rates (Eq. 203) crucially depend on the Kondo factor α , which describes the coupling strength between the excess charge and the nuclear degrees of freedom.

We consider transitions at the donor-acceptor interface such as hole transfer in DIPBI \rightarrow P3HT and electron transfer in P3HT \rightarrow DIPBI as a function of thiophene segment length n (Fig. 3.31). We find the convergence of rates for both holes k_{AB}^h and electrons k_{AB}^e with increasing segment length n . A rising α leads to a decrease in the rates. Moreover, the choice of α scales the order of magnitude in the charge transfer rates. Hence, every selected α results in a different value k_α^{WD} in the asymptotic limit of large n . A selection of different polymers possesses α in the range 1.25 to 6.75 [201].

The Kondo parameter is $\alpha = 3.6$ for rr-P3HT in the literature [201] and $\alpha = 6.75$ in doped rr-P3HT, respectively. From now on, we apply $\alpha = 3.6$ in Weiss-Dorsey rates for hole and electron transfer, respectively (Fig. 3.31, red and blue lines).

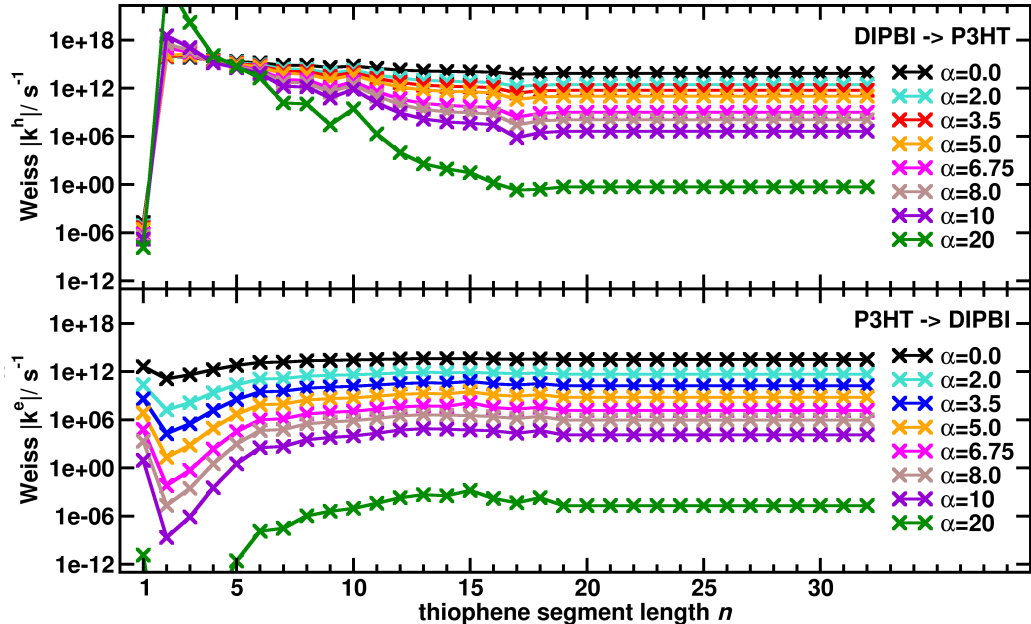


Figure 3.31: Normalised Weiss-Dorsey rates (Eq. 203) as a function of the Kondo parameter α for a DIPBI \rightarrow P3HT hole transfer (above) and P3HT \rightarrow DIPBI electron transfer (below) with thiophene segment length $n \in [1, 32]$. The rates are evaluated using the following parametrisation $|J_{AB}| = 1.0 \text{ eV}$, $\lambda_h^{\text{out}} = 0.157 \text{ eV}$, $\lambda_e^{\text{out}} = 0.132 \text{ eV}$, $|\mathbf{F}^{\text{ext}}| = 0.0 \frac{\text{V}}{\text{m}}$, λ^{in} , ΔE^{in} (B3LYP/6-311G*), $T = 300 \text{ K}$.

In the numeric evaluation of the Jortner rate, the sum over N is limited to $N_{\max} = 20$ iterations (Eq. 204). The intramolecular vibrations for donor and acceptor molecule add to an averaged frequency $\bar{\omega}_{AB}^{\text{int}}$

$$\bar{\omega}_{AB}^{\text{int}} = \frac{1}{2} \left(\frac{1}{N_A^{\text{freq}}} \sum_{i=1}^{N_A^{\text{freq}}} \omega_i^A + \frac{1}{N_B^{\text{freq}}} \sum_{i=1}^{N_B^{\text{freq}}} \omega_i^B \right) = \frac{1}{2} (\bar{\omega}^A + \bar{\omega}^B) \quad (282)$$

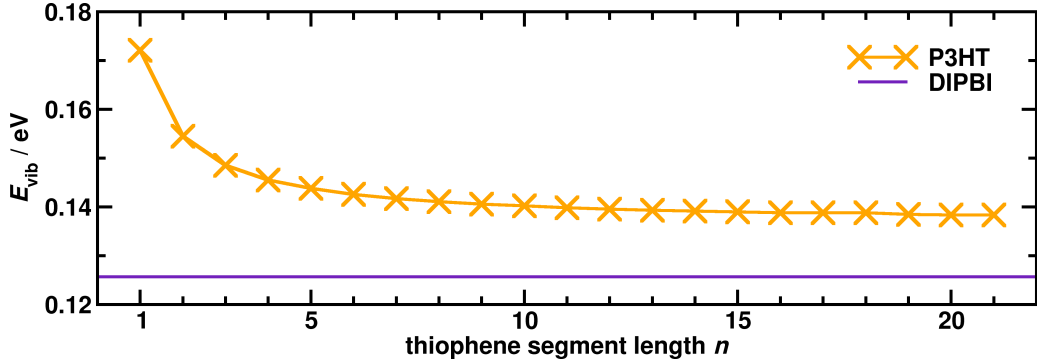


Figure 3.32: Average vibrational energy $E_{\text{vib}} = \hbar\bar{\omega}^{\text{int}}$ for DIPBI and P3HT as a function of the thiophene segment length n as contributions to the Jortner rate.

The average energy contribution for DIPBI and P3HT segments are displayed as a function of the polymer segment length n (Fig. 3.32). They result in $E_{\text{vib}} = \hbar\bar{\omega}^{\text{A}} = 0.126$ eV for DIPBI and $E_{\text{vib}} = 0.138$ to 0.172 eV in P3HT.

Figure 3.33 compares Marcus, Jortner and Weiss-Dorsey charge transfer rates k_{AB} as a function of the site-energy difference ΔE_{AB} . All employed parameters are selected for a hole transfer between two P3HT segments with thiophene segment length $n_A = 6$ and $n_B = 6$. Marcus rates are symmetric concerning the site-energy, which cancels the total reorganization energy ($-\Delta E = \lambda$). Note that a smaller magnitude in the reorganization energy leads to smaller width in the rate distributions and therefore to steeper decays for high $|\Delta E|$. In the case of high energy differences ($|\Delta E| \gg \lambda$), we obtain a rapid decrease in the rates.

One significant difference between the Jortner rates and Marcus rates is the tail of lower rates for endothermic hopping with large, positive ΔE . Higher Jortner rates are obtained for exothermic hopping with a large, negative ΔE , which corresponds to the inverted region in Marcus theory ($-\Delta E > \lambda$). It is known that Marcus theory typically underestimates the magnitude of the rates in the inverted region [186, 298].

Weiss-Dorsey and Jortner rates exhibit an asymmetry, as the charge tunnelling process occurs through a narrower energetic barrier in the inverted regime than in the normal regime. Weiss-Dorsey rates exhibit the highest rates in the regime of enhanced exothermic hopping ($\Delta E \ll -1.0$ eV). Marcus and Weiss-Dorsey rate roughly coincide in the limit of high, positive ΔE . The location of maxima and the magnitude of the maximum rate do not coincide for the three rate types, as they depend on the parameters $\lambda^{\text{in}}, \lambda^{\text{out}}, \alpha, T, E_{\text{vib}}$.

The plot shows the normalised Weiss-Dorsey, Jortner and Marcus charge transfer rates at the donor-acceptor interface in DIPBI \leftrightarrow P3HT as a function of the thiophene segment length n (Fig. 3.34). The rates are evaluated at a fixed charge transfer integral $|J_{\text{AB}}| = 1.0$ eV. The outer-sphere reorganization energies are selected as the mean values $\lambda_{\text{out}}^{\text{h}} = 0.157$ eV, $\lambda_{\text{out}}^{\text{e}} = 0.132$ eV from the distributions in the blend (Fig. A.20). The external field is set to zero.

The Marcus rate for hole transfer k_{AB}^{h} for a DIPBI \rightarrow P3MT ($n = 1$) transition is quite low (Fig. 3.34, iii, red line). It is enhanced for a DIPBI \rightarrow P3MT ($n = 2$) transition. The DIPBI \rightarrow P3MT rates then decrease about 12 orders of magnitude from $n = 3$ to $n = 20$. The rates k_{BA}^{h} for the inverse P3HT \rightarrow DIPBI direction (Fig. 3.34, iii, orange) are moderate for $n = 1$ and $n = 2$ and vanish for $n > 5$, as expected. This finding guarantees predominant hole transport on P3HT.

The DIPBI \rightarrow P3HT Weiss-Dorsey, Jortner and Marcus rates k_{AB}^{e} for electron transfer

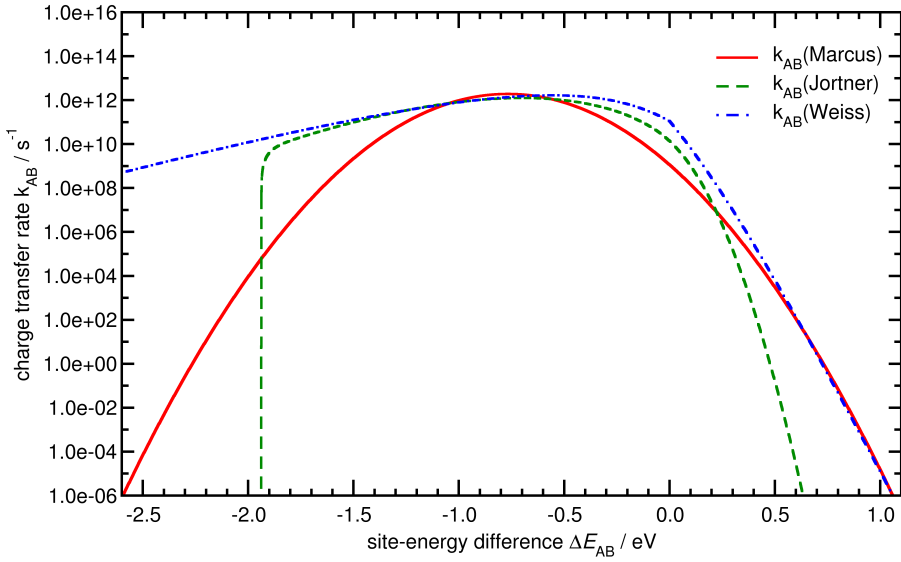


Figure 3.33: Marcus, Jortner and Weiss-Dorsey charge transfer rates k_{AB} as a function of the site-energy difference ΔE_{AB} . The parameters are selected for a hole transfer between two P3HT segments with thiophene segment length $n_A = 6$ and $n_B = 6$: $|J_{AB}| = 0.01$ eV, $\lambda^{in} = 0.61$ eV, $\lambda^{out} = 0.157$ eV, $|\mathbf{F}^{ext}| = 0.0 \frac{\text{V}}{\text{m}}$, $T = 300$ K. The Kondo factor $\alpha = 3.6$ and the average vibrational energy $E_{\text{vib}} = \hbar\bar{\omega}^{\text{int}} = 0.143$ eV are employed.

are always zero (Fig. 3.34, indigo). Furthermore, the Marcus rate transitions are minuscule in the opposite P3HT \rightarrow DIPBI direction and only reach $k_{BA}^e \approx 10^3$ s $^{-1}$ for $n=8$ to 20. This deficiency is an indicator for the failure of the Marcus rate expression for charge-transfer states at the donor-acceptor interface, where $|\Delta E| \gg \lambda$.

This drawback can be overcome when using Weiss-Dorsey rates for the hole and electron transfer in line with a Kondo parameter $\alpha = 3.6$ (Fig. 3.34,i). P3HT \rightarrow DIPBI rates rise gradually with $k_{BA}^e \sim 10^6$ to $\sim 10^{11}$ s $^{-1}$ with increasing n , whereas the rise in opposite direction for DIPBI \rightarrow P3HT is negligible $k_{AB}^e < 10^{-15}$ s $^{-1}$. Weiss-Dorsey DIPBI \rightarrow P3HT hole rates remain at a high level $k_{AB}^h \sim 10^{16}$ s $^{-1}$ for $n = 2$ and $n = 3$, and decrease to $k_{AB}^h \sim 10^{11}$ s $^{-1}$ as n increases. Consequently, the hole transfer rates remain at a higher level than the corresponding electron transfer rates. Moreover, Weiss-Dorsey rates for P3HT \rightarrow DIPBI hole transfer decay with increasing $n > 4$ just like Marcus rates.

The Jortner rates show similar trends as the Weiss-Dorsey rates in the limit of long segments $n > 10$. Normalised DIPBI \rightarrow P3HT hole rates approach $k_{AB}^h \sim 1 \times 10^{12}$ s $^{-1}$, and electrons reach $k_{AB}^e \sim 5 \times 10^{10}$ s $^{-1}$ for P3HT \rightarrow DIPBI. The Jortner rates possess higher values for electron transfer at small segment size $n=2$ to $n=8$ than the other rate types.

Weiss-Dorsey, Jortner and Marcus rate show the same trends of an enhanced hole transfer from DIPBI to P3HT with small segment size. Holes and electrons exhibit an enhanced transfer from P3HT $n=1$ segments to DIPBI, which is in line with the greater tendency to increase the delocalisation of the excess charge.

The normalised Jortner rate for electron transfer is $k_{AB}^e = 2.69 \times 10^{15}$ s $^{-1}$ and for hole transfer $k_{AB}^h = 3.46 \times 10^{15}$ s $^{-1}$ in DIPBI \rightarrow DIPBI, which are similar to the corresponding Marcus rates $k_{AB}^e = 1.14 \times 10^{15}$ s $^{-1}$, and $k_{AB}^h = 1.99 \times 10^{15}$ s $^{-1}$, respectively. In contrast, the normalised Weiss-Dorsey rates are $k_{AB}^e = 1.16 \times 10^{17}$ s $^{-1}$ and $k_{AB}^h = 2.84 \times 10^{17}$ s $^{-1}$, which are two orders of magnitude higher than the associated Jortner and Marcus rates.

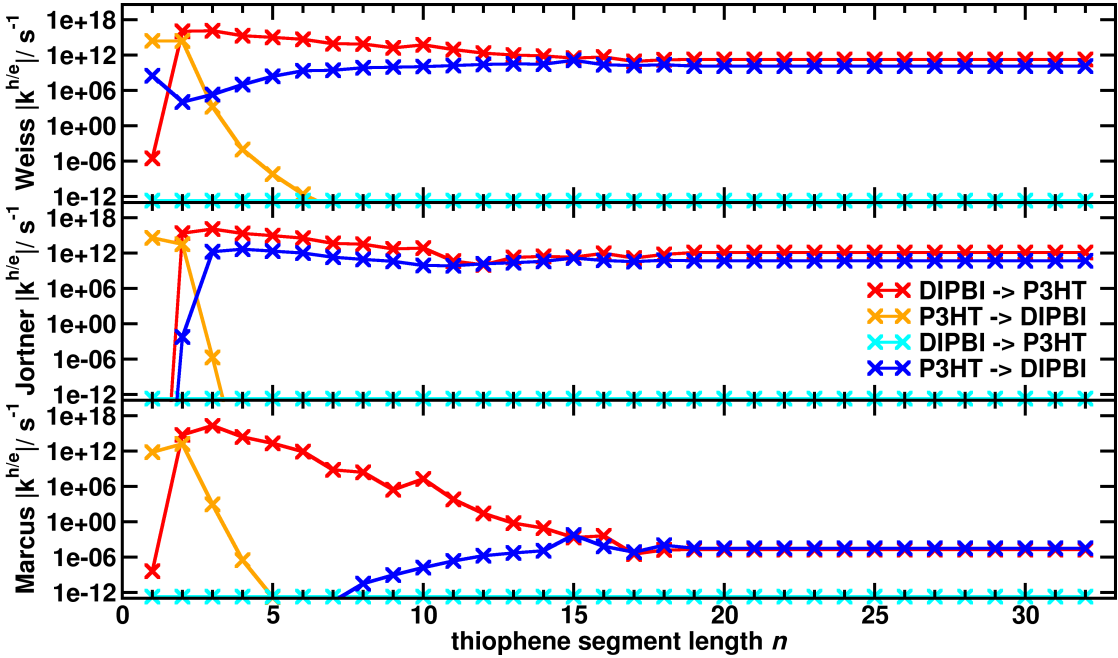


Figure 3.34: Normalised Weiss-Dorsey rates (i), Jortner rates (ii) and Marcus rates (iii) for hole (red/orange) and electron transfer (blue/indigo) at the donor-acceptor interface DIPBI \leftrightarrow P3HT. The rates are depicted as a function of the thiophene segment length of $n \in [1, 32]$. The DIPBI \rightarrow P3HT electron transfer transitions are numerically zero for all rate types. The rates are evaluated using the parameters: $|J_{AB}| = 1.0$ eV, $\lambda_h^{\text{out}} = 0.157$ eV, $\lambda_e^{\text{out}} = 0.132$ eV, $|\mathbf{F}^{\text{ext}}| = 0.0 \frac{\text{V}}{\text{m}}$, λ^{in} , ΔE^{in} (B3LYP/6-311G*), $T = 300$ K, $\alpha = 3.6$.

P3HT \leftrightarrow P3HT transitions are depicted in Fig. 3.35 using normalised intermolecular Weiss-Dorsey rates, Jortner rates and Marcus rates. All three rate types are evaluated for a charge localised at a P3HT segment with $n=4$ and a transfer to a corresponding P3HT n -mer segment and for the opposite direction. In general, all hole and electron rates exhibit enhanced trends for a hopping from a $n=4$ segment to larger segments with $n > 4$, whereas the rates in inverse direction are reduced. Charge transfer from $n < 4$ to the P3HT $n=4$ is enhanced. In conclusion, all rate types reflect the tendency for jumps to target segments with an increased segment size n , which is in line with the expectation of a promoted delocalisation of the excess charge.

Weiss-Dorsey $n=4$ to n -mer hole rates are in the range $k_{4/n}^h = 1.3 \times 10^{16} \text{ s}^{-1}$ to $5.7 \times 10^{15} \text{ s}^{-1}$, where the latter value reflects the long chain limit $n = 32$. Jortner hole transfer rates $k_{4/n}^h = 1.3 \times 10^{16} \text{ s}^{-1}$ to $5.8 \times 10^{15} \text{ s}^{-1}$ and Marcus rates $k_{4/n}^h = 2.0 \times 10^{16} \text{ s}^{-1}$ to $3.8 \times 10^{16} \text{ s}^{-1}$ are approximately at the same range.

The corresponding Weiss-Dorsey electron rates are in the range $k_{4/n}^e = 2.1 \times 10^{16} \text{ s}^{-1}$ to $1.7 \times 10^{15} \text{ s}^{-1}$. Jortner electron rates are $k_{4/n}^e = 1.4 \times 10^{16} \text{ s}^{-1}$ to $2.4 \times 10^{15} \text{ s}^{-1}$, and Marcus rates $k_{4/n}^h = 2.1 \times 10^{16} \text{ s}^{-1}$ to $1.7 \times 10^{14} \text{ s}^{-1}$ are approximately at the same range. In general, all rate types remain at the same orders of magnitudes for $n=4$ to n -mer transitions with $n > 4$. Furthermore, the rates in the inverse direction for a P3HT n -mer \rightarrow 4-mer transition decrease by various orders of magnitude. Weiss-Dorsey rates and Marcus rates decline to similar limits $k_{32/4}^h \sim 1.0 \times 10^0 \text{ s}^{-1}$ and $k_{32/4}^h \sim 5 \times 10^{-3} \text{ s}^{-1}$, whereas Jortner rates decay faster to $k_{32/4}^h \sim 1.0 \times 10^{-18} \text{ s}^{-1}$ and $k_{32/4}^e \sim 1.0 \times 10^{-27} \text{ s}^{-1}$, which are numerically zero.

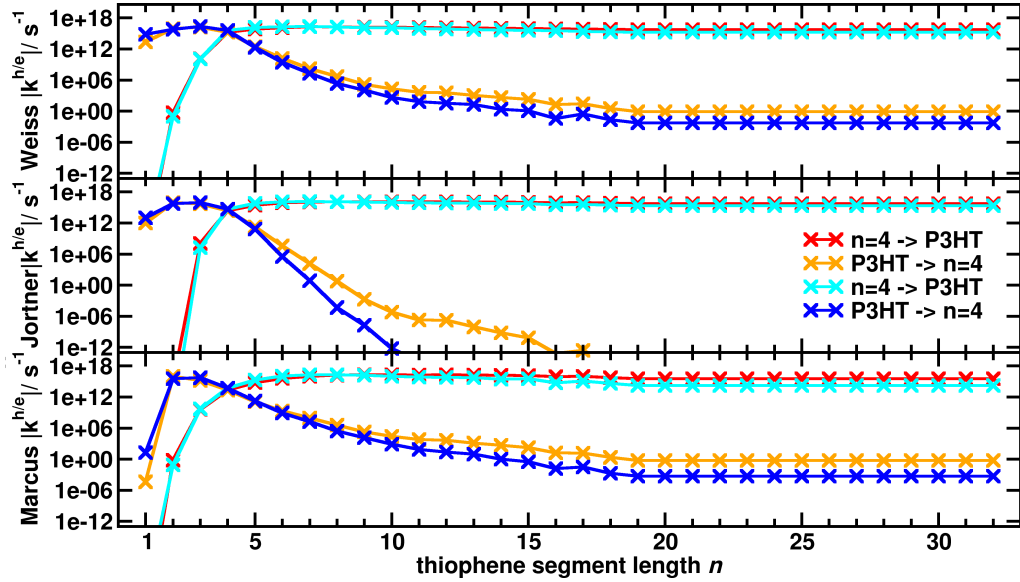


Figure 3.35: Normalised Weiss-Dorsey rates (i), Jortner rates (ii) and Marcus rates (iii) for hole (red/orange) and electron transfer (blue/indigo) for $\text{P3HT } n=4\text{mer} \leftrightarrow \text{P3HT } n\text{-mer}$ transitions with a thiophene segment length $n \in [1, 32]$. The Kondo parameter in the Weiss-Dorsey rates is $\alpha = 3.6$. The rates are evaluated using the parameters: $|J_{AB}| = 1.0 \text{ eV}$, $\lambda_h^{\text{out}} = 0.157 \text{ eV}$, $\lambda_e^{\text{out}} = 0.132 \text{ eV}$, $|\mathbf{F}^{\text{ext}}| = 0.0 \frac{\text{V}}{\text{m}}$, λ^{in} , ΔE^{in} (B3LYP/6-311G*), $T = 300 \text{ K}$.

In conclusion, the Marcus theory fails to describe of charge transfer rates at the donor-acceptor interface in P3HT:DIPBI blends correctly, especially the electron transfer is poorly described. In this case, Weiss-Dorsey and Jortner rates lead to more compelling results. However, all rate types result in similar trends for $\text{P3HT} \leftrightarrow \text{P3HT}$ transitions as a function of the segment length with $n > 2$. Nevertheless, one should keep in mind that these normalised rates use $|J_{AB}| = 1.0 \text{ eV}$ and no outer-sphere contributions. Therefore, they do not take the relative orientation of the molecules inside the morphology into account, which can alter the magnitude of the charge transfer rates significantly. Consequently, caution is required when assessing mobilities from rate-based kMC simulations with interfaces.

